Numer. Math. Theor. Meth. Appl.
doi: 10.4208/nmtma.OA-2025-0089

Vol. **xx**, No. x, pp. 1-39
x 2026

Color Image Segmentation Based on Hue-Saturation Similarity

Wei Wang* and Chengyun Yang

School of Mathematical Sciences, Key Laboratory of Intelligent Computing and Applications (Ministry of Education), Tongji University, Shanghai 200092, China

Received 30 August 2025; Accepted (in revised version) 4 January 2026

Abstract. In this paper, we propose and develop a novel variational model based on hue-saturation similarity and fuzzy membership function for color image segmentation. The main contribution of the proposed model is that we determine different segments by using the similarity of hue and saturation information in hue, saturation, and value color space. We first provide specific definitions of the hue/saturation distance to describe hue-saturation similarity, then formulate a novel data fitting term with an adaptive weight coefficient by using hue-saturation similarity in the proposed energy functional. Two efficient iterative algorithms based on coordinate descent method and alternating direction method of multipliers have been proposed to solve the proposed optimization problem. Theoretically we study the existence of the solution of the proposed model and the convergence of the proposed coordinate descent algorithm. Numerical experimental results demonstrate that the segmentation performance of the proposed model is much better than that of other existing color image segmentation methods.

AMS subject classifications: 65K10, 68U10, 90C26, 68T45, 94A08, 65D18

Key words: Image segmentation, hue, saturation, data fitting, energy minimization, iterative algorithm.

1. Introduction

Image segmentation is the process to partition an image into different regions according to similar characteristics such as intensities, textures, and colors [10]. As one of the well-known variational approaches, region competition [39] is an algorithm de-

*Corresponding author. *Email addresses:* wangw@tongji.edu.cn (W. Wang), 2211185@tongji.edu.cn (C. Yang)

rived by minimizing a generalized Bayes/minimum description length criterion using the variational principle. Geodesic active contour [5] and geodesic active region [25] techniques are proposed based on active contours evolving in time according to intrinsic geometric measures of the images to detect boundaries or textured features. Sparse subspace clustering (SSC) [11] method constructs a self-representation coefficient matrix to represent the relationships between pixels, and then uses spectral clustering to achieve clustering. To overcome the limitations of poor feature representation and computational inefficiency, Wu and Zhao [35] proposed a robust superpixel-based fuzzy SSC algorithm which constructs a unified optimization learning framework through fuzzy C-multiple-means clustering, Zhu *et al.* [40] designed a joint SSC method to capture the structural features in the representation matrix via the L2-norm constraint. The Mumford-Shah model [23, 24] aims to find an optimal piecewise smooth function to approximate the original image, while Chan-Vese model [9] further gives a simplification of the objective function aiming to partition the image domain into several segments with constant intensities. Several convex relaxation approaches [3, 6, 21] unify the Mumford-Shah model and the Rudin-Osher-Fatemi model (ROF) or other regularization term such as L1-norm [36] to overcome the nonconvexity of Mumford-Shah model. Another simplification is to restrict the solution to be piecewise constant, which leads to the so-called piecewise-constant Mumford-Shah model [28, 32]. Grady and Alvino [12] reformulated the corresponding Mumford-Shah model on an arbitrary graph and apply combinatorial optimization to produce a fast, low-energy solution. In [4, 7], the segmentation procedure of the Mumford-Shah model was divided into two steps: getting a smooth image and thresholding it, and in [2, 19], an additional dimension lifting step was proposed for enriching image information. More information on the introduction of the Mumford-Shah model can be found in [31].

Different from the geometric term designed for forcing the total length of the region boundaries, fuzzy segmentation methods such as the multiphase soft segmentation model (SCV) [17, 18] associate image pixels with segmentation regions by using fuzzy membership functions to represent probabilities. Several researches combine fuzzy segmentation methods with active contour methods [1, 13, 37], region competition method [22], denoising regularization [8, 38], Lie group method [29], and other methods to get more robust segmentation results. Meanwhile, bias field (intensity inhomogeneity) may occur in real images with different modalities like nonuniform illumination. Bias correction has been considered in several approaches [15, 16, 26], where a smooth function is proposed to estimate the bias field, and the original image is approximated by the product of a piecewise constant function (segmentation results) and a smooth function (bias field).

Most of the methods mentioned above have rarely considered the situation for color image segmentation. Li *et al.* [16] proposed a Fuzzy Mumford-Shah (FMS) model, which further considers the recovery of the bias field based on the fuzzy segmentation method and the Mumford-Shah model. By calculating the average energy of all channels, FMS can be extended for color image segmentation tasks. Cai *et al.* [2] proposed a smoothing, lifting, and thresholding (SLaT) method with three stages for the mul-

tiphase segmentation of color images. The first smoothing stage is to apply a convex variant of the Mumford-Shah model to each channel to obtain a smooth image. The second lifting stage is to compose a vector-valued image based on the smooth image and its transformed version in a secondary color space, such as the Lab color space [20], to properly handle the color information. The third thresholding stage is to apply multichannel thresholding to the combined vector-valued image to find the segmentation. Jia *et al.* [14] proposed a novel saturation distance of color images, which is used to describe the differences of color pixels through channel coupling. Wang *et al.* [33] introduced the saturation distance into the fuzzy Mumford-Shah functional and proposed the saturation-component based Fuzzy Mumford-Shah model (SFMS) for color image segmentation. Compared to the FMS model, the SFMS model can better segment color images based on color information, and reduce the interference caused by shadows, textures, etc. Recently, Wang *et al.* [34] further proposed a hue based color image restoration model. This observation inspires us to incorporate hue information into color image segmentation models.

In this paper, we propose a novel variational model for color image segmentation based on hue-saturation similarity. Since the hue and saturation components in the hue, saturation, and value (HSV) color space provide more intuitive color information than the RGB space, we introduce hue-saturation similarity by providing specific definitions of the hue and saturation distance in order to capture more color information and describe the inherent correlation among the red, green, and blue channels. In the proposed energy functional, a piecewise smooth image is approximated by the product of a piecewise constant function (segmentation results) and a smooth function (bias field). Meanwhile, a novel data fitting method has been proposed based on the idea of hue-saturation similarity, and an adaptive weight coefficient of the hue similarity term has been incorporated. Specifically, we formulate the fidelity term by minimizing both the hue distance and saturation distance between the input color image and the objective piecewise constant function, and we make use of the saturation part of the input image as the weight of the hue similarity term to balance the role of the hue similarity and saturation similarity adaptively. Numerically, two efficient iterative algorithms including coordinate descent and alternating direction method of multipliers (ADMM) iterations have been proposed to solve the proposed optimization problem. Theoretically, we prove the existence of the model's solution and analyze the convergence of the proposed coordinate descent algorithm. Experiments on both natural and synthetic images show that our model outperforms existing methods in segmentation accuracy.

The rest of this paper is organized as follows. In Section 2, we will introduce the hue-saturation similarity of color images. In Section 3, we will formulate the proposed segmentation model, and study the existence of the solution of the proposed model. In Section 4, we will design two effective and efficient algorithms to solve the proposed minimization problem. In Section 5, we present the comparison of the proposed algorithms. Meanwhile, some experimental results are shown to demonstrate the effectiveness of the proposed model. Finally, some concluding remarks are given in Section 6.

2. Hue-saturation similarity of color images

Wang *et al.* [33] proposed a saturation-component based fuzzy Mumford-Shah model for color image segmentation, which made use of the saturation information. Numerical experiments show that saturation information is very effective for most cases in color image segmentation. However, if we consider more sophisticated color segmentation, such as the segmentation of colors with different hue and similar saturation (e.g. the segmentation of dark red and dark orange), or the segmentation of the same color under different lighting conditions, saturation information is not sufficient. This drives us to further study the role of hue similarity in color segmentation.

2.1. Hue similarity of color images

Assume that

$$\mathbf{f}(x,y) = \big(f_r(x,y), f_g(x,y), f_b(x,y)\big),$$
$$\mathbf{h}(x,y) = \big(h_r(x,y), h_g(x,y), h_b(x,y)\big)$$

are two given color images, then the hue distance of $\mathbf{f}$ and $\mathbf{h}$ can be described as follows, and the hue similarity can be reflected by hue distance,

$$\|\mathbf{f}(x,y)-\mathbf{h}(x,y)\|_H = \begin{cases} |H(\mathbf{f})(x,y) - H(\mathbf{h})(x,y)|, & |H(\mathbf{f})(x,y) - H(\mathbf{h})(x,y)| < \pi, \\ 2\pi - |H(\mathbf{f})(x,y) - H(\mathbf{h})(x,y)|, & |H(\mathbf{f})(x,y) - H(\mathbf{h})(x,y)| \geq \pi, \end{cases}$$

where the hue $H(\mathbf{f})$ can be described as follows:

$$H(\mathbf{f}) = \begin{cases} h(\mathbf{f}), & \beta_1(\mathbf{f}) > 0, \quad \beta_2(\mathbf{f}) \geq 0, \\ \pi - h(\mathbf{f}), & \beta_1(\mathbf{f}) \leq 0, \quad \beta_2(\mathbf{f}) > 0, \\ \pi + h(\mathbf{f}), & \beta_1(\mathbf{f}) < 0, \quad \beta_2(\mathbf{f}) \leq 0, \\ 2\pi - h(\mathbf{f}), & \beta_1(\mathbf{f}) \geq 0, \quad \beta_2(\mathbf{f}) < 0, \end{cases}$$

$$h(\mathbf{f}) = \tan^{-1}\left(\frac{\sqrt{3}|f_g - f_b|}{|2f_r - f_g - f_b|}\right), \tag{2.1}$$

$$\beta_1(\mathbf{f}) = \operatorname{sign}(2f_r - f_g - f_b), \quad \beta_2(\mathbf{f}) = \operatorname{sign}(f_g - f_b). \tag{2.2}$$

The detailed derivation of $h(\cdot)$ and $H(\cdot)$ can be found in [34].

2.2. Saturation similarity of color images

As is discussed in [14], the saturation distance of $\mathbf{f}$ and $\mathbf{h}$ can be described as follows, and the saturation similarity can be reflected by saturation distance,

$$\|\mathbf{f}(x,y) - \mathbf{h}(x,y)\|_S = \frac{1}{3}\left\| \begin{bmatrix} 2 & -1 & -1 \\ -1 & 2 & -1 \\ -1 & -1 & 2 \end{bmatrix} \begin{bmatrix} f_r(x,y) - h_r(x,y) \\ f_g(x,y) - h_g(x,y) \\ f_b(x,y) - h_b(x,y) \end{bmatrix} \right\|_2.$$

3. Color image segmentation by hue-saturation similarity

3.1. The formulation of the proposed model

In this paper, we propose to use the following model for color image:

$$\mathbf{U}(x) = g(x)\mathbf{c}_i + \mathbf{n}(x), \quad x \in \Omega_i,$$

where $U : \Omega \to \mathbb{R}^d$ with $\Omega \in \mathbb{R}^2$ being a bounded open connected set is the given image to be segmented. Here $d = 1$ is for gray-scale image, $d = 3$ is for RGB color image, and $d > 3$ is for many cases such as hyperspectral image [27] and medical image [30]. We focus on color image ($d = 3$) in this paper. The smooth function g represents the bias field which is introduced to deal with illumination inhomogeneity for color images, and it is assumed to be valued around 1. $\mathbf{c}_i$ is a constant, $\mathbf{n}$ represents the noise, and Ω_i refers to a segment of the partition. Based on the idea of fuzzy membership function and the definition of hue-saturation similarity, we propose the following hue-saturation fuzzy (HSF) segmentation model:

$$\begin{aligned} E(\alpha_i, g, \mathbf{c}) = \lambda \sum_{i=1}^{N} \int_\Omega \left(\|\mathbf{U} - g\mathbf{c}_i\|_S^2 + \rho_1 \|\mathbf{U} - \mathbf{c}_i\|_S^2 + \rho_2 \left(\|\mathbf{U}\|_S \|\mathbf{U} - \mathbf{c}_i\|_H \right)^2 \right) \alpha_i^p dx \\ + \mu \int_\Omega |\nabla g|^2 dx + \sum_{i=1}^{N} \int_\Omega |\nabla \alpha_i| dx \end{aligned} \tag{3.1}$$

with the input image $\mathbf{U}$ partitioned into N regions. $\mathbf{U} = (U_1, U_2, U_3), \mathbf{c}_i = (c_{i1}, c_{i2}, c_{i3})$ refers to the RGB channels of input image and the i-th part of the segment result, α_i is the fuzzy membership function which is constrained by

$$0 \le \alpha_i \le 1, \quad \sum_{i=1}^{N} \alpha_i = 1. \tag{3.2}$$

In the proposed functional, we consider L^2 norm of the gradient to model the smooth bias function g, and we apply total variation to model the fuzzy membership function α_i. For the data fitting term, we make use of $\|\mathbf{U} - \mathbf{c}_i\|_S$ and $\|\mathbf{U} - g\mathbf{c}_i\|_S$ to illustrate the saturation similarity. As one of the most important contributions, we introduce $\|\mathbf{U} - \mathbf{c}_i\|_H$ to illustrate the hue similarity. The intention of the proposed model is to handle the segmentation of colors with similar hue plus different saturation or different hue plus similar saturation. We give a simple example in Fig. 1 to illustrate the effect of the hue similarity term. First, we can see that the red part is divided into dark red and light red (similar hue plus different saturation), and we tend to segment the entire red part in this case. However, we see from the result that only using the saturation similarity is not sufficient to give the expected segmentation for the case of one color (same hue) with different saturation. Meanwhile, we also expect to separate the yellow part and the red part (different hue plus similar saturation) in the segmentation result, but using only saturation similarity can not meet our expectation neither.

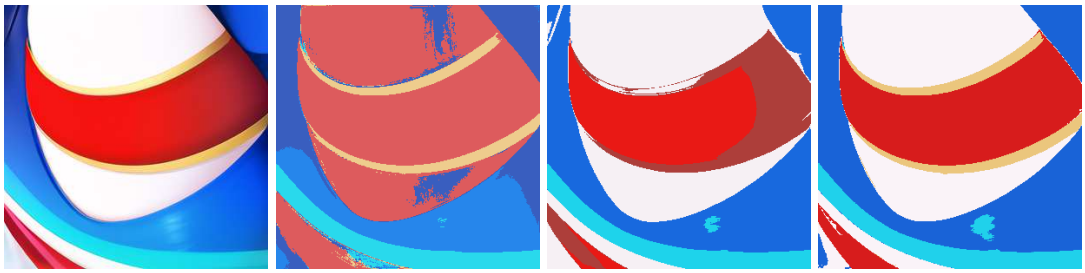

Figure 1: Left to right: the input image; the segmentation result by using HSF without the saturation weight; the segmentation result by using only saturation similarity; the segmentation result by using HSF with the saturation weight. The parameters of HSF: $(\lambda, \rho_1, \rho_2, \mu) = (1\text{e-}2, 1\text{e-}3, 1\text{e}2, 2\text{e}5)$.

After introducing the hue similarity term in the proposed HSF model, we see that the segmentation result is exactly what we expected. Another important contribution of the proposed model is that we introduce an adaptive weight coefficient of the hue similarity term, i.e., we make use of the saturation part of the input image $\|\mathbf{U}\|_S$ as the weight of $\|\mathbf{U} - \mathbf{c}_i\|_H$. The mechanism is as follows, hue similarity plays a major role where the saturation is high, while saturation similarity plays a major role where the saturation is low. For the area where the saturation is moderate, hue similarity and saturation similarity work at the same time. In Fig. 1, we can see that without $\|\mathbf{U}\|_S$, the white background with light red color and the red region are segmented into the same area. This is mainly because that without $\|\mathbf{U}\|_S$, the effect of the hue similarity is over-amplified where the saturation is low. Therefore, we introduce the saturation weight to balance the role of the hue similarity and saturation similarity adaptively.

3.2. The existence of the solution

Noting that if $(g, \mathbf{c}_i)$ is a solution, $(kg, \mathbf{c}_i/k)$ is also a solution with a scaling factor k when minimizing the functional in (3.1). Then the uniqueness of the solution is not available. Therefore, we set the scale of $\mathbf{c}_i$ by using the following formula:

$$c_{ij} = \begin{cases} \displaystyle\int_\Omega U_j \alpha_i^p dx \left(\int_\Omega \alpha_i^p dx \right)^{-1}, & \displaystyle\int_\Omega \alpha_i^p dx > 0, \\ 0, & \displaystyle\int_\Omega \alpha_i^p dx = 0, \end{cases} \quad j = 1, 2, 3, \tag{3.3}$$

which gives the mean value of image $\mathbf{U}$ in Ω_i.

Suppose Ω is a bounded open subset of R^{2m} with a positive integer m. Let $\mathbb{B}^m$ denote the closed united ball in $\mathbb{R}^m$ and $\mathcal{K}^m = \mathcal{C}^1(\Omega, \mathbb{B}^{2m})$ be the set of continuously differentiable and bounded functions from the compact support in Ω to $\mathbb{B}^{2m}$. We define $\mathbb{BV}(\Omega)$ as follows:

$$\mathbb{BV}(\Omega) = \left\{ u \in L^1(\Omega); \int_\Omega |Du| = \sup_{\xi \in \mathcal{K}^m} \left\{ \int_\Omega u \mathrm{div} \xi dx \right\} < \infty \right\},$$

where Du is called the distributional gradient of u. Assume that $U_j \in L^\infty(\Omega)$, $j = 1, 2, 3$, the energy functional (3.1) is well-defined in the following admissible set:

$$\Lambda = \left\{\alpha_i \in \mathbb{BV}(\Omega),\ i = 1 : N,\ \text{satisfies (3.2)};\ g \in W^{1,2}(\Omega);\ \mathbf{c} \in \mathbb{R}^N \times \mathbb{R}^N \times \mathbb{R}^N\right\}.$$

Now we give the existence result of the minimizer of functional (3.1).

Theorem 3.1. *Assume that $U_j \in L^\infty(\Omega)$ and $U_j \geq 0, j = 1, 2, 3$, then for fixed parameters $N, \lambda, \rho_1, \rho_2, \mu$, there exists a minimizer of* (3.1) *in the admissible set* Λ.

Proof. As $E \geq 0$, the infimum of E exists. Let $\{(\alpha_i^n, g^n, \mathbf{c}^n)\} \subseteq \Lambda$ be a minimizing sequence of E, which gives $E(\alpha_i^n, g^n, \mathbf{c}^n) \to \inf E(\alpha_i, g, \mathbf{c})$ as $n \to \infty$.

Notice that as taking $g = 0, \alpha_1 = 1, \alpha_i = 0\ (i = 2, \ldots, N), c_{1j} = \int_\Omega U_j dx/|\Omega|$ $(j = 1, 2, 3), \mathbf{c}_i = \mathbf{0}\ (i = 2, \ldots, N)$, E will be a finite value, so $\inf E(\alpha_i, g, \mathbf{c})$ is finite. Then upto a subsequence of $\{(\alpha_i^n, g^n, \mathbf{c}^n)\}$, which still denoted by $\{(\alpha_i^n, g^n, \mathbf{c}^n)\}$, there exists a constant $M_1 \geq 0$ satisfies that $E(\alpha_i^n, g^n, \mathbf{c}^n) \leq M_1$, then each term is bounded. Specially,

$$\lambda \int_\Omega \|\mathbf{U} - g\mathbf{c}_i\|_S^2 (\alpha_i^n)^p dx \leq M_1, \quad \mu \int_\Omega |\nabla g^n|^2 dx \leq M_1, \quad \int_\Omega |\nabla \alpha_i^n| dx \leq M_1. \tag{3.4}$$

Since $0 \leq \alpha_i^n \leq 1$,

$$\|\alpha_i^n\|_{L^1(\Omega)} = \int_\Omega \alpha_i^n dx \leq |\Omega|.$$

Together with (3.4), we deduce that α_i^n is uniformly bounded in $\mathbb{BV}(\Omega)$ for $i = 1, \ldots, N$. By using the compactness of $\mathbb{BV}$ space, there is a subsequence of $\{\alpha_i^n\}$ which still denoted by $\{\alpha_i^n\}$, and a function $\alpha_i^* \in \mathbb{BV}(\Omega)$, satisfies that

$$\begin{aligned} &\alpha_i^n \to \alpha_i^* \qquad \text{strongly in } L^1(\Omega), \quad \alpha_i^n \to \alpha_i^* \quad \text{a.e.} \quad x \in \Omega, \\ &\nabla \alpha_i^n \to \nabla \alpha_i^* \quad \text{in the sense of measure.} \end{aligned}$$

By using the lower-semicontinuity of total variation, we have

$$\int_\Omega |\nabla \alpha_i^*| dx \leq \liminf_{n \to \infty} \int_\Omega |\nabla \alpha_i^n| dx. \tag{3.5}$$

Meanwhile, α_i^* satisfies (3.2). By using formula (3.3), we can deduce that

$$0 \leq c_{ij}^n \leq \|U_j\|_{L^\infty(\Omega)},$$

which means $\{c_{ij}^n\}$ is also bounded. So there is a subsequence of $\{c_{ij}^n\}$ which still denoted by $\{c_{ij}^n\}$, satisfies that

$$c_{ij}^n \to c_{ij}^*, \quad c_{ij}^* = \begin{cases} \displaystyle\int_\Omega U_j (\alpha_i^*)^p dx \left(\int_\Omega (\alpha_i^*)^p dx \right)^{-1}, & \displaystyle\int_\Omega (\alpha_i^*)^p dx > 0, \\ 0, & \displaystyle\int_\Omega (\alpha_i^*)^p dx = 0, \end{cases} \quad j = 1, 2, 3.$$

We unfold the first inequality of (3.4) and derive that

$$\begin{aligned}
&\int_\Omega \left[(2U_1 - U_2 - U_3) - g^n(2c_{i1}^n - c_{i2}^n - c_{i3}^n)\right]^2 (\alpha_i^n)^p dx \le M_1,\\
&\int_\Omega \left[(-U_1 + 2U_2 - U_3) - g^n(-c_{i1}^n + 2c_{i2}^n - c_{i3}^n)\right]^2 (\alpha_i^n)^p dx \le M_1,\\
&\int_\Omega \left[(-U_1 - U_2 + 2U_3) - g^n(-c_{i1}^n - c_{i2}^n + 2c_{i3}^n)\right]^2 (\alpha_i^n)^p dx \le M_1.
\end{aligned}$$

As U_1, U_2, U_3 are constants and c_{ij}^n is bounded, unless $U_1 = U_2 = U_3$, which means the given color image has degraded into a grayscale image, $\max\{(2c_{i1}^n - c_{i2}^n - c_{i3}^n)^2, (-c_{i1}^n + 2c_{i2}^n - c_{i3}^n)^2, (-c_{i1}^n - c_{i2}^n + 2c_{i3}^n)^2\}$ must be positive, which derives that

$$\int_\Omega (g^n)^2 (\alpha_i^n)^p dx \le M_2$$

for some fixed $M_2 > 0$. By using [16, Lemma 3.2], there exists $\rho(x) \in L^2(\Omega)$ such that

- $\rho(x) \ge 0$ and $\int_\Omega \rho dx = 1$;
- for some fixed $M_3 > 0$, $\left|\int_\Omega g^n \rho dx\right| \le M_3$.

By using the generalized Poincaré inequality on Ω, we get

$$\|g^n - \langle g^n, \rho\rangle\|_{L^2(\Omega)} \le K \|\nabla g^n\|_{L^2(\Omega)}$$

for some fixed K, which means $\|g^n\|_{L^2(\Omega)}$ can be controlled by $\|\nabla g^n\|_{L^2(\Omega)}$. Together with (3.4), we can easily derive that $\|g^n\|_{W^{1,2}(\Omega)}$ is uniformly bounded. Then there is a subsequence of $\{g^n\}$ which still denoted by $\{g^n\}$, and a function $g^* \in W^{1,2}(\Omega)$, satisfies that

$$g^n \to g^* \quad \text{strongly in } L^2(\Omega), \quad g^n \to g^* \quad \text{a.e. } x \in \Omega, \quad g^n \to g^* \quad \text{weakly in } W^{1,2}(\Omega).$$

By using the lower-semicontinuity, we have

$$\int_\Omega |\nabla g^*|^2 dx \le \liminf_{n\to\infty} \int_\Omega |\nabla g^n|^2 dx. \tag{3.6}$$

Finally, by using Fatou's Lemma, we derive that

$$\begin{aligned}
&\int_\Omega \left(|\mathbf{U} - g^*\mathbf{c}_i^*|_S^2 + \rho_1 |\mathbf{U} - \mathbf{c}_i^*|_S^2 + \rho_2 \left(\|\mathbf{U}\|_S |\mathbf{U} - \mathbf{c}_i^*|_H\right)^2\right) (\alpha_i^*)^p dx\\
&\le \liminf_{n\to\infty} \int_\Omega \left(|\mathbf{U} - g^n\mathbf{c}_i^n|_S^2 + \rho_1 |\mathbf{U} - \mathbf{c}_i^n|_S^2 + \rho_2 \left(\|\mathbf{U}\|_S |\mathbf{U} - \mathbf{c}_i^n|_H\right)^2\right) (\alpha_i^n)^p dx.
\end{aligned} \tag{3.7}$$

Combining the inequalities (3.5)-(3.7), considering a suitable subsequence, we have

$$E(\alpha^*, g^*, \mathbf{c}^*) \le \liminf_{n\to\infty} E(\alpha^n, g^n, \mathbf{c}^n) = \inf E(\alpha, g, \mathbf{c}),$$

which proves that $(\alpha^*, g^*, \mathbf{c}^*) \in \Lambda$ is a minimizer of E. □

4. Numerical algorithm

4.1. Coordinate descent based algorithm

In this section, we present an alternative minimization algorithm to solve the proposed optimization problem, which is a generalization of the algorithm proposed in [16]. We conclude it as the following Algorithm 4.1.

Algorithm 4.1

1. Initialization: randomly set α_i^0, set $g^0 = 1$, set $\mathbf{c}_i^0$ by using formula (3.3).
2. For fixed $\mathbf{c}_i^k, \alpha_i^k$, update g^{k+1} by solving

$$g^{k+1} = \arg\min_{g} \sum_{i=1}^{N} \frac{\lambda}{2} \int_{\Omega} \left\|\mathbf{U} - g\mathbf{c}_i^k\right\|_S^2 (\alpha_i^k)^p dx + \frac{\mu}{2} \int_{\Omega} |\nabla g|^2 dx. \tag{4.1}$$

3. For fixed $g^{k+1}, \mathbf{c}_i^k$, update α_i^{k+1} by solving

$$\alpha_i^{k+1} = \arg\min_{\alpha_i} \frac{\lambda}{2} \sum_{i=1}^{N} \int_{\Omega} d_i^k \alpha_i^p dx + \sum_{i=1}^{N} \int_{\Omega} |\nabla \alpha_i| dx, \tag{4.2}$$

where

$$d_i^k = \left\|\mathbf{U} - g^{k+1}\mathbf{c}_i^k\right\|_S^2 + \rho_1 \left\|\mathbf{U} - \mathbf{c}_i^k\right\|_S^2 + \rho_2 \left(\|\mathbf{U}\|_S \left\|\mathbf{U} - \mathbf{c}_i^k\right\|_H\right)^2.$$

4. For fixed α_i^{k+1}, g^{k+1}, update $\mathbf{c}_i^{k+1}$ by using formula (3.3).
5. Go back to Step 2 until $|\alpha_i^{k+1} - \alpha_i^k|^2 / |\alpha_i^k|^2 < \epsilon$ for fixed ϵ.

4.1.1. Updating g

We first give the Euler-Lagrange equation of the optimization problem with respect to g (4.1). By letting $\mathbf{q} = \mathbf{U} - g\mathbf{c}_i^k$, then the Euler-Lagrange equation can be given as

$$\sum_{i=1}^{N} \frac{\lambda}{9} \Big[(2q_1 - q_2 - q_3)\big(2c_{i1}^k - c_{i2}^k - c_{i3}^k\big) + (2q_2 - q_1 - q_3)\big(2c_{i2}^k - c_{i1}^k - c_{i3}^k\big) + (2q_3 - q_1 - q_2)\big(2c_{i3}^k - c_{i1}^k - c_{i2}^k\big) \Big] \alpha_i^p + \mu \triangle g = 0.$$

By letting

$$J_1 = \frac{1}{3} \sum_{i=1}^{N} \Big(2U_1 c_{i1}^k + 2U_2 c_{i2}^k + 2U_3 c_{i3}^k - U_1 c_{i2}^k - U_1 c_{i3}^k - U_2 c_{i1}^k - U_2 c_{i3}^k - U_3 c_{i1}^k - U_3 c_{i2}^k \Big) (\alpha_i^k)^p,$$

$$J_2 = \frac{2}{3}\sum_{i=1}^{N}\left((c_{i1}^k)^2 + (c_{i2}^k)^2 + (c_{i3}^k)^2 - c_{i1}^k c_{i2}^k - c_{i1}^k c_{i3}^k - c_{i2}^k c_{i3}^k\right)(\alpha_i^k)^p,$$

the above Euler-Lagrange equation can be simplified as follows:

$$\lambda(J_1 - J_2 g) + \mu\triangle g = 0. \tag{4.3}$$

We consider the following discrete scheme of $\triangle g$:

$$(\triangle g)_{x,y} = g_{x+1,y} + g_{x-1,y} + g_{x,y+1} + g_{x,y-1} - 4g_{x,y}$$

to provide the following Gauss-Seidel iteration formula for solving g subproblem with periodic boundary condition,

$$g_{x,y}^{k,t+1} = \frac{\mu(g_{x+1,y}^{k,t} + g_{x-1,y}^{k,t+1} + g_{x,y+1}^{k,t} + g_{x,y-1}^{k,t+1}) + \lambda(J_1)_{x,y}}{4\mu + \lambda(J_2)_{x,y}},$$

where x, y denotes the grid, t is the inner iteration index.

4.2. Updating α_i

In this section, we fix $g, \mathbf{c}_i$, and update α_i. We set $p = 2$ in practice. The optimization problem with respect to α_i (4.2) can be written as,

$$\min_{\alpha_i} E(\alpha_i) = \frac{\lambda}{2}\sum_{i=1}^{N}\int_\Omega d_i\alpha_i^2 dx + \sum_{i=1}^{N}\int_\Omega |\nabla\alpha_i| dx,$$

subject to $0 \le \alpha_i \le 1, \sum_{i=1}^N \alpha_i = 1$. We use the following iterative method introduced in [16] to solve the above minimization problem:

$$\begin{cases} \mathbf{y}_i^{t+1} = \min\left\{\frac{1}{\tau}, |\mathbf{y}_i^t + \tau\nabla\alpha_i^t|\right\}\frac{\mathbf{y}_i^t + \tau\nabla\alpha_i^t}{|\mathbf{y}_i^t + \tau\nabla\alpha_i^t|}, \\ v_i^{t+1} = \alpha_i^t - \theta\nabla^\top\mathbf{y}_i^{t+1}, \\ \alpha_i^{t+1} = \min\left\{\max\left\{\frac{v_i^{t+1}}{1+\lambda\theta d_i} - \frac{\sum_{j=1}^N (v_j^{t+1}/(1+\lambda\theta d_j)) - 1}{\sum_{j=i}^N (1+\lambda\theta d_i)/(1+\lambda\theta d_j)}, 0\right\}, 1\right\}. \end{cases}$$

Here $\mathbf{y}_i$ and v_i are two auxiliary variables introduced as the intermediate iterative variables, where i indicates i-th phase same as the subscript of α_i, and t represents the t-th iteration. Parameters τ and θ only influence the convergence speed. We only iterate once in each iterative step from α_i^k to α_i^{k+1} in practice.

4.3. Convergence analysis

We first give the following lemma to illustrate that $\mathbf{c}_i^{k+1}$ given by formula (3.3) is one of the minimizers of $\mathbf{c}$ subproblem in Algorithm 4.1.

Lemma 4.1. *If μ (which is the weight of ∇g) is set to be large enough, and there is a positive constant $s > 0$ such that $|\mathbf{U}|_S \geq s$ holds on Ω. Then with a proper number of image segmentation regions N, formula* (3.3) *gives an approximate solution of the following minimization problem:*

$$\arg\min_{\mathbf{c}} \left\{ E_c(\mathbf{c}) = \sum_{i=1}^{N} \int_{\Omega} \Big(\|\mathbf{U} - g^{k+1}\mathbf{c}_i\|_S^2 + \rho_1 \|\mathbf{U} - \mathbf{c}_i\|_S^2 + \rho_2 \left(\|\mathbf{U}\|_S \|\mathbf{U} - \mathbf{c}_i\|_H \right)^2 \Big) \alpha_i^p dx \right\}. \tag{4.4}$$

Proof. We consider the following three minimization problem:

$$\begin{aligned}
&\arg\min_{\mathbf{c}} \left\{ E_1(\mathbf{c}) = \sum_{i=1}^{N} \int_{\Omega} \|\mathbf{U} - \mathbf{c}_i\|_S^2 \alpha_i^p dx \right\}, \\
&\arg\min_{\mathbf{c}} \left\{ E_2(\mathbf{c}) = \sum_{i=1}^{N} \int_{\Omega} \|\mathbf{U} - g^{k+1}\mathbf{c}_i\|_S^2 \alpha_i^p dx \right\}, \\
&\arg\min_{\mathbf{c}} \left\{ E_3(\mathbf{c}) = \sum_{i=1}^{N} \int_{\Omega} \left(\|\mathbf{U}\|_S \|\mathbf{U} - \mathbf{c}_i\|_H \right)^2 \alpha_i^p dx \right\}.
\end{aligned}$$

For energy functional $E_1(\mathbf{c})$, we calculate the first-order variation as follows:

$$\frac{\delta E_1(\mathbf{c})}{\delta \mathbf{c}} = \frac{2}{3} \begin{bmatrix} \sum_{i=1}^{N} \int_{\Omega} \big((2c_{i1} - c_{i2} - c_{i3}) - (2U_1 - U_2 - U_3) \big) \alpha_i^p dx \\ \sum_{i=1}^{N} \int_{\Omega} \big((2c_{i2} - c_{i3} - c_{i1}) - (2U_2 - U_3 - U_1) \big) \alpha_i^p dx \\ \sum_{i=1}^{N} \int_{\Omega} \big((2c_{i3} - c_{i1} - c_{i2}) - (2U_3 - U_1 - U_2) \big) \alpha_i^p dx \end{bmatrix}.$$

It is clear that when $\mathbf{c}_i$ satisfies

$$\int_{\Omega} c_{ij} \alpha_i^p dx = \int_{\Omega} U_j \alpha_i^p dx,$$

which is consist with formula (3.3), we get that

$$\left. \frac{\delta E_1(\mathbf{c})}{\delta \mathbf{c}} \right|_{\mathbf{c}=\mathbf{c}^{k+1}} = \mathbf{0}. \tag{4.5}$$

For energy functional $E_2(\mathbf{c})$, we calculate the first-order variation as follows:

$$\frac{\delta E_2(\mathbf{c})}{\delta \mathbf{c}} = \frac{2}{3}\begin{bmatrix} \sum_{i=1}^{N}\int_\Omega \big(g^{k+1}(2c_{i1}-c_{i2}-c_{i3})-(2U_1-U_2-U_3)\big)\alpha_i^p dx \\ \sum_{i=1}^{N}\int_\Omega \big(g^{k+1}(2c_{i2}-c_{i3}-c_{i1})-(2U_2-U_3-U_1)\big)\alpha_i^p dx \\ \sum_{i=1}^{N}\int_\Omega \big(g^{k+1}(2c_{i3}-c_{i1}-c_{i2})-(2U_3-U_1-U_2)\big)\alpha_i^p dx \end{bmatrix}.$$

We find that if $\mathbf{c}_i$ is given by formula (3.3), then we get

$$\left.\frac{\delta E_2(\mathbf{c})}{\delta \mathbf{c}}\right|_{\mathbf{c}=\mathbf{c}^{k+1}} = \frac{2}{3}\begin{bmatrix} \sum_{i=1}^{N}\int_\Omega (g^{k+1}-1)(2U_1-U_2-U_3)\alpha_i^p dx \\ \sum_{i=1}^{N}\int_\Omega (g^{k+1}-1)(2U_2-U_1-U_3)\alpha_i^p dx \\ \sum_{i=1}^{N}\int_\Omega (g^{k+1}-1)(2U_3-U_1-U_2)\alpha_i^p dx \end{bmatrix}.$$

We sum all pixels of both side of Eq. (4.3), we then have

$$\lambda\sum_{i,j}(J_1-J_2 g)+\mu\sum_{i,j}\triangle g = 0.$$

If $\mu\to\infty$, g is forced to be flat, which means there exists a constant c, $g(i,j)=c$ for all pixels. By the definition of J_1, J_2 given in Section 4.1.1, the formula (3.3), it is easy to deduce that $\sum_{i,j} J_1 = \sum_{i,j} J_2$. Now the equation is degenerated into

$$\lambda\sum_{i,j}(J_1-J_1 c) = 0,$$

which gives $c=1$. Therefore, by setting μ large enough, we can assume that $|g^{k+1}-1|$ is a small quantity ϵ_1. Also, as $U_i\in[0,1], \alpha_i\in[0,1]$ are bounded, then

$$|(2U_1-U_2-U_3)\alpha_i^p|\le 4,\quad |(2U_2-U_1-U_3)\alpha_i^p|\le 4,\quad |(2U_3-U_1-U_2)\alpha_i^p|\le 4.$$

Therefore, we can deduce that

$$\left|\left.\frac{\delta E_2(\mathbf{c})}{\delta \mathbf{c}}\right|_{\mathbf{c}=\mathbf{c}^{k+1}}\right| \le \left(\frac{8}{3}\sum_{i=1}^{N}\int_\Omega \epsilon_1 dx\right)\cdot\mathbf{1}. \tag{4.6}$$

For energy functional $E_3(\mathbf{c})$, by setting proper number of image segmentation regions N, we can assume that for each segmentation region Ω_i, the hue and saturation of each pixel are almost the same, which gives the following assumption:

$$\|\mathbf{U}-\mathbf{c}_i\|_H = |h(\mathbf{c}_i)-h(\mathbf{U})|,\quad \|\mathbf{U}\|_S^2 = S^2+\epsilon_2,$$

where S is a constant refers to the approximate saturation of Ω_i, and ϵ_2 is a small quantity. By this assumption, we can derive the first-order variation as follows:

$$\frac{\delta E_3(\mathbf{c})}{\delta \mathbf{c}} = 2\sum_{i=1}^{N} \frac{\delta h(\mathbf{c}_i)}{\delta \mathbf{c}_i} \left(S^2 \int_\Omega \big(h(\mathbf{c}_i) - h(\mathbf{U})\big)\alpha_i^p dx + \int_\Omega \epsilon_2 \big(h(\mathbf{c}_i) - h(\mathbf{U})\big)\alpha_i^p dx \right).$$

We rewrite $h(\mathbf{U})$ through the first order Taylor expansion,

$$\begin{aligned}\int_\Omega h(\mathbf{U})\alpha_i^p dx &= \int_\Omega \left(h(\mathbf{c}_i) + \frac{\delta h(\mathbf{c})}{\delta \mathbf{c}}\bigg|_{\mathbf{c}=\mathbf{c}_i} (\mathbf{U}-\mathbf{c}_i) + o(\mathbf{U}-\mathbf{c}_i) \right) \alpha_i^p dx \\ &= \int_\Omega h(\mathbf{c}_i)\alpha_i^p dx + \frac{\delta h(\mathbf{c})}{\delta \mathbf{c}}\bigg|_{\mathbf{c}=\mathbf{c}_i} \int_\Omega (\mathbf{U}-\mathbf{c}_i)\,\alpha_i^p dx + \int_\Omega \epsilon_3 \alpha_i^p dx,\end{aligned}$$

where ϵ_3 is a small quantity regarded as $o(\mathbf{U}-\mathbf{c}_i)$. It is clear that formula (3.3) satisfies

$$\int_\Omega \left(\mathbf{U} - \mathbf{c}_i^{k+1}\right) \alpha_i^p dx = \mathbf{0},$$

then we have

$$\int_\Omega h(\mathbf{U})\alpha_i^p dx = \int_\Omega h\big(\mathbf{c}_i^{k+1}\big)\alpha_i^p dx + \int_\Omega \epsilon_3 \alpha_i^p dx,$$

then we can get that

$$\frac{\delta E_3(\mathbf{c})}{\delta \mathbf{c}}\bigg|_{\mathbf{c}=\mathbf{c}^{k+1}} = 2\sum_{i=1}^{N} \frac{\delta h(\mathbf{c})}{\delta \mathbf{c}}\bigg|_{\mathbf{c}=\mathbf{c}_i^{k+1}} \left(\int_\Omega \epsilon_2 \left(h(\mathbf{c}_i^{k+1}) - h(\mathbf{U}) \right) \alpha_i^p dx - S^2 \int_\Omega \epsilon_3 \alpha_i^p dx \right).$$

Similarly, we can also rewrite $\|\mathbf{U}\|_S^2$ as follows:

$$\int_\Omega \|\mathbf{U}\|_S^2 \alpha_i^p dx = \int_\Omega \big\|\mathbf{c}_i^{k+1}\big\|_S^2 \alpha_i^p dx + \int_\Omega \epsilon_4 \alpha_i^p dx,$$

where ϵ_4 is a small quantity regarded as $o(\mathbf{U}-\mathbf{c}_i)$. Using the assumption $\|\mathbf{U}\|_S \geq s > 0$, we can deduce that

$$\begin{aligned}\big\|\mathbf{c}_i^{k+1}\big\|_S^2 &= \int_\Omega \|\mathbf{U}\|_S^2 \alpha_i^p dx \left(\int_\Omega \alpha_i^p dx \right)^{-1} - \int_\Omega \epsilon_4 \alpha_i^p dx \left(\int_\Omega \alpha_i^p dx \right)^{-1} \\ &\geq s^2 - \int_\Omega \epsilon_4 \alpha_i^p dx \left(\int_\Omega \alpha_i^p dx \right)^{-1} > \frac{s^2}{2}.\end{aligned}$$

In [34], the detailed calculation of $\delta h(\mathbf{c})/\delta \mathbf{c}$ is given as

$$\frac{\delta h(\mathbf{c})}{\delta \mathbf{c}}\bigg|_{\mathbf{c}=\mathbf{c}_i^{k+1}} = \frac{2\beta_1\beta_2}{\sqrt{3}\|\mathbf{c}_i^{k+1}\|_S^2} \begin{bmatrix} c_{i3}^{k+1} - c_{i2}^{k+1} \\ c_{i1}^{k+1} - c_{i3}^{k+1} \\ c_{i2}^{k+1} - c_{i1}^{k+1} \end{bmatrix},$$

where β_1, β_2 have the same meaning in formula (2.1). As $c_{ij} \in [0,1], h(\mathbf{c}) \in [0, \pi/2]$ are bounded, we have

$$\left|\frac{\delta h(\mathbf{c})}{\delta \mathbf{c}}\Big|_{\mathbf{c}=\mathbf{c}^{k+1}}\right| \leq \frac{8}{\sqrt{3}s^2} \cdot \mathbf{1},$$
$$\left|\frac{\delta E_3(\mathbf{c})}{\delta \mathbf{c}}\Big|_{\mathbf{c}=\mathbf{c}^{k+1}}\right| \leq \sum_{i=1}^{N} \frac{16}{\sqrt{3}s^2}\left(\pi \int_\Omega \epsilon_2 dx + S^2 \int_\Omega \epsilon_3 dx\right) \cdot \mathbf{1}. \tag{4.7}$$

Combine the formulas (4.5)-(4.7), we can finally get that formula (3.3) satisfies

$$\begin{aligned}\left|\frac{\delta E_c(\mathbf{c})}{\delta \mathbf{c}}\Big|_{\mathbf{c}=\mathbf{c}^{k+1}}\right| &= \left|\left(\rho_1 \frac{\delta E_1(\mathbf{c})}{\delta \mathbf{c}} + \frac{\delta E_2(\mathbf{c})}{\delta \mathbf{c}} + \rho_2 \frac{\delta E_3(\mathbf{c})}{\delta \mathbf{c}}\right)\Big|_{\mathbf{c}=\mathbf{c}^{k+1}}\right| \\ &\leq \sum_{i=1}^{N}\left(\frac{8}{3}\int_\Omega \epsilon_1 dx + \frac{16\rho_2\pi}{\sqrt{3}s^2}\int_\Omega \epsilon_2 dx + \frac{16\rho_2 S^2}{\sqrt{3}s^2}\int_\Omega \epsilon_3 dx\right) \cdot \mathbf{1} \leq \epsilon \mathbf{M},\end{aligned}$$

where

$$\mathbf{M} = N|\Omega|\left(\frac{8}{3} + \frac{16\rho_2\pi}{\sqrt{3}s^2} + \frac{16\rho_2 S^2}{\sqrt{3}s^2}\right) \cdot \mathbf{1},$$

ϵ is a fixed small quantity which is larger than $\epsilon_1, \epsilon_2, \epsilon_3$ and is not depend on Ω. $|\Omega|$ is the measure of Ω, which is also bounded. It is clear that $\mathbf{M}$ is finite, and the value is not depend on the iteration k. Therefore, for proper parameter selection, formula (3.3) is one of the approximate solutions of the minimization problem. □

By Lemma 4.1, we can reasonably assume that

$$\mathbf{c}_i^{k+1} = \arg\min_{\mathbf{c}} \left\{E\big(\alpha_i^{k+1}, g^{k+1}, \mathbf{c}\big)\right\}.$$

Combine it with the following results in Algorithm 4.1:

$$g^{k+1} = \arg\min_{g} \left\{E\big(\alpha_i^{k}, g, \mathbf{c}^{k}\big)\right\},$$
$$\alpha_i^{k+1} = \arg\min_{\alpha_i} \left\{E\big(\alpha_i, g^{k+1}, \mathbf{c}^{k}\big)\right\},$$

we can derive the following convergence result of the proposed algorithm.

Theorem 4.1. *Let $(\alpha_i^k, g^k, \mathbf{c}_i^k)$ be the sequence derived from Algorithm* 4.1*, then $(\alpha_i^k, g^k, \mathbf{c}_i^k)$ converges to $(\alpha_i^*, g^*, \mathbf{c}_i^*) \in \Lambda$ (up to a subsequence) which is a coordinate minimizer of the proposed energy E, i.e., for any $(\alpha_i, g, \mathbf{c}_i) \in \Lambda$, we have*

$$E(\alpha_i^*, g^*, \mathbf{c}_i^*) \leq E(\alpha_i^*, g, \mathbf{c}_i^*),$$
$$E(\alpha_i^*, g^*, \mathbf{c}_i^*) \leq E(\alpha_i^*, g^*, \mathbf{c}_i),$$
$$E(\alpha_i^*, g^*, \mathbf{c}_i^*) \leq E(\alpha_i, g^*, \mathbf{c}_i^*).$$

Proof. We first show the following inequality:

$$E\big(\alpha_i^{k+1}, g^{k+1}, \mathbf{c}_i^{k+1}\big) \le E\big(\alpha_i^{k+1}, g^{k+1}, \mathbf{c}_i^{k}\big) \le E\big(\alpha_i^{k}, g^{k+1}, \mathbf{c}_i^{k}\big) \le E\big(\alpha_i^{k}, g^{k}, \mathbf{c}_i^{k}\big). \quad (4.8)$$

Remark that the sequence $(\alpha_i^k, g^k, \mathbf{c}_i^k)$ satisfies

$$\mathbf{c}_i^{k+1} = \arg\min_{\mathbf{c}} \Big\{ E\big(\alpha_i^{k+1}, g^{k+1}, \mathbf{c}\big) \Big\},$$

which means

$$E\big(\alpha_i^{k+1}, g^{k+1}, \mathbf{c}_i^{k+1}\big) \le E\big(\alpha_i^{k+1}, g^{k+1}, \mathbf{c}\big), \quad \forall \mathbf{c} \in \mathbb{R}^d.$$

Specifically, we choose $\mathbf{c}$ as $\mathbf{c}_i^k$, then we have

$$E\big(\alpha_i^{k+1}, g^{k+1}, \mathbf{c}_i^{k+1}\big) \le E\big(\alpha_i^{k+1}, g^{k+1}, \mathbf{c}_i^{k}\big),$$

which gives the first part of inequality (4.8). The following parts can be deduced by using similar arguments.

From the above inequality, $E(\alpha_i^k, g^k, \mathbf{c}_i^k)$ is bounded. As discussed in Theorem 3.1, we can find subsequences (which are still noted as $(\alpha_i^k, g^k, \mathbf{c}_i^k)$) in the admissible set such that

$$\begin{array}{lll}
\alpha_i^n \to \alpha_i^* & \text{strongly in } L^1(\Omega), & \alpha_i^n \to \alpha_i^* \quad \text{a.e.} \quad x \in \Omega, \\
\nabla\alpha_i^n \to \nabla\alpha_i^* & \text{in the sense of measure}, & \\
g^n \to g^* & \text{strongly in } L^2(\Omega), & g^n \to g^* \quad \text{a.e.} \quad x \in \Omega, \\
 & & g^n \to g^* \quad \text{weakly in } W^{1,2}(\Omega), \\
\mathbf{c}_i^k \to \mathbf{c}_i^* & &
\end{array}$$

with $(\alpha_i^*, g^*, \mathbf{c}_i^*) \in \Lambda$. Recall that $E(\alpha_i^k, g^k, \mathbf{c}_i^k) \ge 0$, then there exists $m \ge 0$ such that

$$m = \lim_{k\to\infty} E\big(\alpha_i^k, g^k, \mathbf{c}_i^k\big).$$

We then show the following inequalities:

$$\begin{aligned}
&E\big(\alpha_i^{k+1}, g^{k+1}, \mathbf{c}_i^{k+1}\big) \le E\big(\alpha_i^{k}, g^{k}, \mathbf{c}_i^{k}\big) \le E\big(\alpha_i^{k}, g^{k}, \mathbf{c}_i^{*}\big), \\
&E\big(\alpha_i^{k+1}, g^{k+1}, \mathbf{c}_i^{k+1}\big) \le E\big(\alpha_i^{k}, g^{k+1}, \mathbf{c}_i^{k}\big) \le E\big(\alpha_i^{k}, g^{*}, \mathbf{c}_i^{k}\big), \\
&E\big(\alpha_i^{k+1}, g^{k+1}, \mathbf{c}_i^{k+1}\big) \le E\big(\alpha_i^{k}, g^{k}, \mathbf{c}_i^{k}\big) \le E\big(\alpha_i^{k}, g^{k}, \mathbf{c}_i^{k-1}\big) \le E\big(\alpha_i^{*}, g^{k}, \mathbf{c}_i^{k-1}\big).
\end{aligned}$$

Remark that the sequence $(\alpha_i^k, g^k, \mathbf{c}_i^k)$ satisfies

$$\mathbf{c}_i^{k} = \arg\min_{\mathbf{c}} \Big\{ E\big(\alpha_i^{k}, g^{k}, \mathbf{c}\big) \Big\},$$

which means

$$E\big(\alpha_i^{k}, g^{k}, \mathbf{c}_i^{k}\big) \le E(\alpha_i^{k}, g^{k}, \mathbf{c}), \quad \forall \mathbf{c} \in \mathbb{R}^d.$$

Specifically, we choose $\mathbf{c}$ as $\mathbf{c}_i^*$ and combine it with inequality (4.8), we then have

$$E\big(\alpha_i^{k+1}, g^{k+1}, \mathbf{c}_i^{k+1}\big) \leq E\big(\alpha_i^k, g^k, \mathbf{c}_i^k\big) \leq E\big(\alpha_i^k, g^k, \mathbf{c}_i^*\big).$$

Other inequalities can be deduced by using similar arguments. By summing the above inequalities, we can derive that

$$3E\big(\alpha_i^{k+1}, g^{k+1}, \mathbf{c}_i^{k+1}\big) \leq E\big(\alpha_i^k, g^*, \mathbf{c}_i^k\big) + E\big(\alpha_i^k, g^k, \mathbf{c}_i^*\big) + E\big(\alpha_i^*, g^k, \mathbf{c}_i^{k-1}\big).$$

By rewriting the right-hand side, we obtain that

$$\begin{aligned}
&E\big(\alpha_i^k, g^*, \mathbf{c}_i^k\big) + E\big(\alpha_i^k, g^k, \mathbf{c}_i^*\big) + E\big(\alpha_i^*, g^k, \mathbf{c}_i^{k-1}\big) \\
&= E\big(\alpha_i^*, g^*, \mathbf{c}_i^*\big) + 2E\big(\alpha_i^k, g^k, \mathbf{c}_i^k\big) \\
&\quad + \lambda \sum_{i=1}^N \int_\Omega \left(\|\mathbf{U} - g^* \mathbf{c}_i^k\|_S^2 + \rho_1 \|\mathbf{U} - \mathbf{c}_i^k\|_S^2 + \rho_2 \left(\|\mathbf{U}\|_S \|\mathbf{U} - \mathbf{c}_i^k\|_H \right)^2 \right) (\alpha_i^k)^p dx \\
&\quad + \lambda \sum_{i=1}^N \int_\Omega \left(\|\mathbf{U} - g^k \mathbf{c}_i^*\|_S^2 + \rho_1 \|\mathbf{U} - \mathbf{c}_i^*\|_S^2 + \rho_2 \left(\|\mathbf{U}\|_S \|\mathbf{U} - \mathbf{c}_i^*\|_H \right)^2 \right) (\alpha_i^k)^p dx \\
&\quad + \lambda \sum_{i=1}^N \int_\Omega \Big(\|\mathbf{U} - g^k \mathbf{c}_i^{k-1}\|_S^2 + \rho_1 \|\mathbf{U} - \mathbf{c}_i^{k-1}\|_S^2 \\
&\qquad\qquad + \rho_2 \left(\|\mathbf{U}\|_S \|\mathbf{U} - \mathbf{c}_i^{k-1}\|_H \right)^2 \Big) (\alpha_i^*)^p dx \\
&\quad - \lambda \sum_{i=1}^N \int_\Omega \left(\|\mathbf{U} - g^* \mathbf{c}_i^*\|_S^2 + \rho_1 \|\mathbf{U} - \mathbf{c}_i^*\|_S^2 + \rho_2 \left(\|\mathbf{U}\|_S \|\mathbf{U} - \mathbf{c}_i^*\|_H \right)^2 \right) (\alpha_i^*)^p dx \\
&\quad - 2\lambda \sum_{i=1}^N \int_\Omega \left(\|\mathbf{U} - g^k \mathbf{c}_i^k\|_S^2 + \rho_1 \|\mathbf{U} - \mathbf{c}_i^k\|_S^2 + \rho_2 \left(\|\mathbf{U}\|_S \|\mathbf{U} - \mathbf{c}_i^k\|_H \right)^2 \right) (\alpha_i^k)^p dx.
\end{aligned}$$

By using the convergence results listed above, when $k \to \infty$, we can easily deduce that

$$\begin{aligned}
&\sum_{i=1}^N \int_\Omega \left(\|\mathbf{U} - g^k \mathbf{c}_i^k\|_S^2 + \rho_1 \|\mathbf{U} - \mathbf{c}_i^k\|_S^2 + \rho_2 \left(\|\mathbf{U}\|_S \|\mathbf{U} - \mathbf{c}_i^k\|_H \right)^2 \right) (\alpha_i^k)^p dx \\
&\to \sum_{i=1}^N \int_\Omega \left(\|\mathbf{U} - g^* \mathbf{c}_i^*\|_S^2 + \rho_1 \|\mathbf{U} - \mathbf{c}_i^*\|_S^2 + \rho_2 \left(\|\mathbf{U}\|_S \|\mathbf{U} - \mathbf{c}_i^*\|_H \right)^2 \right) (\alpha_i^*)^p, \\
&\sum_{i=1}^N \int_\Omega \left(\|\mathbf{U} - g^* \mathbf{c}_i^k\|_S^2 + \rho_1 \|\mathbf{U} - \mathbf{c}_i^k\|_S^2 + \rho_2 \left(\|\mathbf{U}\|_S \|\mathbf{U} - \mathbf{c}_i^k\|_H \right)^2 \right) (\alpha_i^k)^p dx \\
&\to \sum_{i=1}^N \int_\Omega \left(\|\mathbf{U} - g^* \mathbf{c}_i^*\|_S^2 + \rho_1 \|\mathbf{U} - \mathbf{c}_i^*\|_S^2 + \rho_2 \left(\|\mathbf{U}\|_S \|\mathbf{U} - \mathbf{c}_i^*\|_H \right)^2 \right) (\alpha_i^*)^p, \\
&\sum_{i=1}^N \int_\Omega \left(\|\mathbf{U} - g^k \mathbf{c}_i^{k-1}\|_S^2 + \rho_1 \|\mathbf{U} - \mathbf{c}_i^{k-1}\|_S^2 + \rho_2 \left(\|\mathbf{U}\|_S \|\mathbf{U} - \mathbf{c}_i^{k-1}\|_H \right)^2 \right) (\alpha_i^*)^p dx
\end{aligned}$$

$$\to \sum_{i=1}^{N} \int_{\Omega} \left(\|\mathbf{U} - g^* \mathbf{c}_i^*\|_S^2 + \rho_1 \|\mathbf{U} - \mathbf{c}_i^*\|_S^2 + \rho_2 \left(\|\mathbf{U}\|_S \|\mathbf{U} - \mathbf{c}_i^*\|_H \right)^2 \right) (\alpha_i^*)^p.$$

Therefore, let $k \to \infty$ we have

$$3m \leq E\big(\alpha_i^*, g^*, \mathbf{c}_i^*\big) + 2m,$$

i.e.,

$$E\big(\alpha_i^*, g^*, \mathbf{c}_i^*\big) \geq m.$$

Combining with the lower-semicontinuity result, we finally get that

$$m = \liminf_{k \to \infty} E\big(\alpha_i^k, g^k, \mathbf{c}_i^k\big) \geq E\big(\alpha_i^*, g^*, \mathbf{c}_i^*\big) \geq m,$$

which leads to

$$E\big(\alpha_i^*, g^*, \mathbf{c}_i^*\big) = m.$$

Then for any $(\alpha_i, g, \mathbf{c}_i) \in \Lambda$, we have

$$\begin{aligned}
3E\big(\alpha_i^{k+1}, g^{k+1}, \mathbf{c}_i^{k+1}\big) &\leq E\big(\alpha_i^k, g, \mathbf{c}_i^k\big) + E\big(\alpha_i^k, g^k, \mathbf{c}_i^*\big) + E\big(\alpha_i^*, g^k, \mathbf{c}_i^{k-1}\big), \\
3E\big(\alpha_i^{k+1}, g^{k+1}, \mathbf{c}_i^{k+1}\big) &\leq E\big(\alpha_i^k, g^*, \mathbf{c}_i^k\big) + E\big(\alpha_i^k, g^k, \mathbf{c}_i\big) + E\big(\alpha_i^*, g^k, \mathbf{c}_i^{k-1}\big), \\
3E\big(\alpha_i^{k+1}, g^{k+1}, \mathbf{c}_i^{k+1}\big) &\leq E\big(\alpha_i^k, g^*, \mathbf{c}_i^k\big) + E\big(\alpha_i^k, g^k, \mathbf{c}_i^*\big) + E\big(\alpha_i, g^k, \mathbf{c}_i^{k-1}\big).
\end{aligned}$$

We can get the following results by using similar arguments above

$$\begin{aligned}
E\big(\alpha_i^*, g^*, \mathbf{c}_i^*\big) &\leq E\big(\alpha_i^*, g, \mathbf{c}_i^*\big), \\
E\big(\alpha_i^*, g^*, \mathbf{c}_i^*\big) &\leq E\big(\alpha_i^*, g^*, \mathbf{c}_i\big), \\
E\big(\alpha_i^*, g^*, \mathbf{c}_i^*\big) &\leq E\big(\alpha_i, g^*, \mathbf{c}_i^*\big).
\end{aligned}$$

The proof is complete. □

4.4. ADMM based algorithm

In this subsection, we present an ADMM based algorithm to solve the proposed optimization problem. We first consider the following equivalent minimization problem:

$$\begin{aligned}
&E(\alpha_i, g, \mathbf{c}, z_i, v_i, w) \\
&= \frac{\lambda}{2} \sum_{i=1}^{N} \int_{\Omega} \left(\|\mathbf{U} - w\mathbf{c}_i\|_S^2 + \rho_1 \|\mathbf{U} - \mathbf{c}_i\|_S^2 + \rho_2 \left(\|\mathbf{U}\|_S \|\mathbf{U} - \mathbf{c}_i\|_H \right)^2 \right) z_i^p dx \\
&\quad + \frac{\mu}{2} \int_{\Omega} |\nabla g|^2 dx + \sum_{i=1}^{N} \int_{\Omega} |\nabla \alpha_i| dx + \sum_{i=1}^{N} \tau(v_i), \\
&\text{subject to} \quad z_i = \alpha_i, \quad w = g, \quad v_i = \alpha_i, \quad \sum_{i=1}^{N} z_i = 1,
\end{aligned}$$

where

$$\tau(v) = \begin{cases} 0, & \text{if} \quad 0 \le v \le 1, \\ +\infty, & \text{otherwise.} \end{cases}$$

We then give the augmented Lagrange function as follows:

$$\begin{aligned}
&E(\alpha_i, g, \mathbf{c}, z_i, v_i, w, \gamma_i, \theta_i, \gamma, \theta) \\
&= \frac{\lambda}{2}\sum_{i=1}^{N}\int_\Omega \left(\|\mathbf{U} - w\mathbf{c}_i\|_S^2 + \rho_1\|\mathbf{U} - \mathbf{c}_i\|_S^2 + \rho_2\left(\|\mathbf{U}\|_S\|\mathbf{U} - \mathbf{c}_i\|_H\right)^2\right) z_i^p dx + \sum_{i=1}^{N}\tau(v_i) \\
&\quad + \frac{\mu}{2}\int_\Omega |\nabla g|^2 dx + \sum_{i=1}^{N}\int_\Omega |\nabla \alpha_i| dx + \sum_{i=1}^{N}\int_\Omega \gamma_i \cdot (z_i - \alpha_i)\, dx + \frac{\beta_1}{2}\sum_{i=1}^{N}\int_\Omega |z_i - \alpha_i|^2 dx \\
&\quad + \int_\Omega \gamma \cdot (w - g)\, dx + \frac{\beta_2}{2}\int_\Omega |w - g|^2 dx + \sum_{i=1}^{N}\int_\Omega \eta_i \cdot (v_i - \alpha_i)\, dx \\
&\quad + \frac{\beta_3}{2}\sum_{i=1}^{N}\int_\Omega |v_i - \alpha_i|^2 dx + \int_\Omega \eta \cdot \left(\sum_{i=1}^{N} z_i - 1\right) dx + \frac{\beta_4}{2}\sum_{i=1}^{N}\int_\Omega \left|\sum_{i=1}^{N} z_i - 1\right|^2 dx,
\end{aligned}$$

where $\gamma_i, \eta_i, \gamma, \eta$ are the dual variables corresponding to the constraints, $\beta_1, \beta_2, \beta_3, \beta_4$ are the penalty parameters. We conclude the ADMM iteration as the following Algorithm 4.2.

Algorithm 4.2

1. Initialization of main variables: randomly set α_i^0, set $g^0 = 1$, set $\mathbf{c}_i^0$ by using formula (3.3).
2. Initialization of auxiliary variables: set $z_i^0 = \alpha_i^0, v_i^0 = \alpha_i^0, w^0 = g^0 = 1$.
3. Initialization of dual variables: set $\gamma_i^0 = 0, \eta_i^0 = 0, \gamma^0 = 0, \eta^0 = 0$.

Block 1

4. For other fixed variables, update α_i^{k+1} by solving

$$\begin{aligned}
\alpha_i^{k+1} = \arg\min_{\alpha_i} &\int_\Omega |\nabla \alpha_i| dx + \frac{\beta_1}{2}\int_\Omega \left|z_i^k - \alpha_i + \frac{\gamma_i^k}{\beta_1}\right|^2 dx \\
&+ \frac{\beta_3}{2}\int_\Omega \left|v_i^k - \alpha_i + \frac{\eta_i^k}{\beta_3}\right|^2 dx.
\end{aligned} \tag{4.9}$$

5. For other fixed variables, update g^{k+1} by solving

$$g^{k+1} = \arg\min_g \frac{\mu}{2}\int_\Omega |\nabla g|^2 dx + \frac{\beta_2}{2}\int_\Omega \left|w^k - g + \frac{\gamma^k}{\beta_2}\right|^2 dx. \tag{4.10}$$

6. For other fixed variables, update $\mathbf{c}_i^{k+1}$ by using

$$c_{ij} = \begin{cases} \displaystyle\int_\Omega U_j z_i^p dx \left(\int_\Omega z_i^p dx\right)^{-1}, & \displaystyle\int_\Omega z_i^p dx > 0, \\ 0, & \displaystyle\int_\Omega z_i^p dx = 0, \end{cases} \qquad j = 1, 2, 3,$$

which is a same form discussed in formula (3.3).

Block 2

7. For other fixed variables, update z_i^{k+1} by solving

$$\mathbf{z}^{k+1} = \arg\min_{\mathbf{z}} \frac{\lambda}{2} \sum_{i=1}^{N} \int_{\Omega} d_i^k z_i^p dx + \frac{\beta_1}{2} \sum_{i=1}^{N} \int_{\Omega} \left| z_i - \alpha_i^{k+1} + \frac{\gamma_i^k}{\beta_1} \right|^2 dx + \frac{\beta_4}{2} \int_{\Omega} \left| \sum_{i=1}^{N} z_i - 1 + \frac{\eta^k}{\beta_4} \right|^2 dx, \tag{4.11}$$

where

$$d_i^k = \left\| \mathbf{U} - w^k \mathbf{c}_i^{k+1} \right\|_S^2 + \rho_1 \left\| \mathbf{U} - \mathbf{c}_i^{k+1} \right\|_S^2 + \rho_2 \left(\|\mathbf{U}\|_S \|\mathbf{U} - \mathbf{c}_i^{k+1}\|_H \right)^2.$$

8. For other fixed variables, update v_i^{k+1} by solving

$$v_i^{k+1} = \arg\min_{v_i} \sum_{i=1}^{N} \tau(v_i) + \frac{\beta_3}{2} \sum_{i=1}^{N} \int_{\Omega} \left| v_i - \alpha_i^{k+1} + \frac{\eta_i^k}{\beta_3} \right|^2 dx. \tag{4.12}$$

Block 3

9. For other fixed variables, update w^{k+1} by solving

$$w^{k+1} = \arg\min_{w} \frac{\lambda}{2} \sum_{i=1}^{N} \int_{\Omega} \left\| \mathbf{U} - w \mathbf{c}_i^{k+1} \right\|_S^2 (z_i^{k+1})^p dx + \frac{\beta_2}{2} \int_{\Omega} \left| w - g^{k+1} + \frac{\gamma^k}{\beta_2} \right|^2 dx. \tag{4.13}$$

Dual variables updates

10. For other fixed variables, update $\gamma_i, \gamma, \eta_i, \eta$ by

$$\begin{aligned} \gamma_i^{k+1} &= \gamma_i^k + \beta_1 \left(z_i^{k+1} - \alpha_i^{k+1} \right), \\ \gamma^{k+1} &= \gamma^k + \beta_2 \left(w^{k+1} - g^{k+1} \right), \\ \eta_i^{k+1} &= \eta_i^k + \beta_3 \left(v_i^{k+1} - \alpha_i^{k+1} \right), \\ \eta^{k+1} &= \eta^k + \beta_4 \left(\sum_{i=1}^{N} z_i^{k+1} - 1 \right). \end{aligned}$$

11. Go back to Step 4 until $|\alpha_i^{k+1} - \alpha_i^k|^2 / |\alpha_i^k|^2 < \epsilon$ for fixed ϵ.

4.4.1. Updating α_i

For α_i sub-problem (4.9), which is a traditional total variation problem with a regularization term plus two L_2 data fidelity terms. We apply ADMM iteration to solve it here.

Let $\mathbf{h}_i = \nabla\alpha_i$, set $\boldsymbol{\tau}_i$ be the auxiliary variables and θ be the penalty parameter, the argumented Lagrange function is given as,

$$\min_{\alpha_i,\mathbf{h}_i,\boldsymbol{\tau}_i} \int_\Omega |\mathbf{h}_i| dx + \frac{\beta_1}{2}\int_\Omega \left| z_i^k - \alpha_i + \frac{\gamma_i^k}{\beta_1}\right|^2 dx + \frac{\beta_3}{2}\int_\Omega \left| v_i^k - \alpha_i + \frac{\eta_i^k}{\beta_3}\right|^2 dx + \frac{\theta}{2}\int_\Omega \left|\mathbf{h}_i - \nabla\alpha_i + \frac{\boldsymbol{\tau}_i}{\theta}\right|^2 dx.$$

Let t be the inner ADMM iteration index. For α_i sub-problem

$$\min_{\alpha_i} \frac{\beta_1}{2}\int_\Omega \left| z_i^k - \alpha_i + \frac{\gamma_i^k}{\beta_1}\right|^2 dx + \frac{\beta_3}{2}\int_\Omega \left| v_i^k - \alpha_i + \frac{\eta_i^k}{\beta_3}\right|^2 dx + \frac{\theta}{2}\int_\Omega \left|\mathbf{h}_i - \nabla\alpha_i + \frac{\boldsymbol{\tau}_i}{\theta}\right|^2 dx$$

it is equivalent to solve the following equation:

$$(\beta_1 + \beta_3 + \theta\nabla^\top\cdot\nabla)\alpha_i = \beta_1\left(z_i^k + \frac{\gamma_i^k}{\beta_1}\right) + \beta_3\left(v_i^k + \frac{\eta_i^k}{\beta_3}\right) + \theta\nabla^\top\cdot\left(\mathbf{h}_i^t + \frac{\boldsymbol{\tau}_i^t}{\theta}\right),$$

which can be quickly solved by using Fast Fourier transform (FFT),

$$\alpha_i^{t+1} = \mathcal{F}^{-1}\left(\frac{\begin{array}{c}\beta_1\mathcal{F}(z_i^k + \gamma_i^k/\beta_1) + \beta_3\mathcal{F}(v_i^k + \eta_i^k/\beta_3) \\ + \theta\mathcal{F}(\nabla_1)^*\mathcal{F}(h_{i1}^t + \boldsymbol{\tau}_i^t/\theta) + \theta\mathcal{F}(\nabla_2)^*\mathcal{F}(h_{i2}^t + \boldsymbol{\tau}_i^t/\theta)\end{array}}{\beta_1 + \beta_3 + \theta\left(\mathcal{F}(\nabla_1)^*\mathcal{F}(\nabla_1) + \mathcal{F}(\nabla_2)^*\mathcal{F}(\nabla_2)\right)}\right).$$

$\mathbf{h}_i$ sub-problem

$$\min_{\mathbf{h}_i} \int_\Omega |\mathbf{h}_i| dx + \frac{\theta}{2}\int_\Omega \left|\mathbf{h}_i - \nabla\alpha_i^{t+1} + \frac{\boldsymbol{\tau}_i^t}{\theta}\right|^2 dx,$$

has the following closed-form solution:

$$\mathbf{h}_i = \max\left\{0, \left|\nabla\alpha_i^{t+1} - \frac{\boldsymbol{\tau}_i^t}{\theta}\right| - \frac{1}{\theta}\right\}\frac{\nabla\alpha_i^{t+1} - \boldsymbol{\tau}_i^t/\theta}{\left|\nabla\alpha_i^{t+1} - \boldsymbol{\tau}_i^t/\theta\right|}.$$

$\boldsymbol{\tau}_i$ is updated by

$$\boldsymbol{\tau}_i^{t+1} = \boldsymbol{\tau}_i^t + \theta\big(\mathbf{h}_i^{t+1} - \nabla\alpha_i^{t+1}\big).$$

4.4.2. Updating g

By similar method discussed in Section 4.1.1, we first give the Euler-Lagrange equation of the optimization problem with respect to g (4.10)

$$\beta_2\left(g - \left(w^k + \frac{\gamma^k}{\beta_2}\right)\right) - \mu\triangle g = 0.$$

Using the following discrete scheme of $\triangle g$:

$$(\triangle g)_{x,y} = g_{x+1,y} + g_{x-1,y} + g_{x,y+1} + g_{x,y-1} - 4g_{x,y},$$

we provide the Gauss-Seidel iteration formula for solving g subproblem with periodic boundary condition,

$$g_{x,y}^{k,t+1} = \frac{\mu(g_{x+1,y}^{k,t} + g_{x-1,y}^{k,t+1} + g_{x,y+1}^{k,t} + g_{x,y-1}^{k,t+1}) + (\beta_2 w^k + \gamma^k)_{x,y}}{4\mu + \beta_2},$$

where x, y denotes the grid, t is the inner iteration index.

4.4.3. Updating z_i

For z_i sub-problem (4.11), we only consider the case of $p = 2$. The first order optimal conditions are given as

$$\lambda d_i^k z_i + \beta_1 \left(z_i - \alpha_i^{k+1} + \frac{\gamma_i^k}{\beta_1} \right) + \beta_4 \left(\sum_{j=1}^{N} z_j - 1 + \frac{\eta^k}{\beta_4} \right) = 0, \quad \forall i = 1, \ldots, N,$$

which gives a linear system of equations. Let $A_i = \lambda d_i^k + \beta_1, B_i = \beta_1 \alpha_i^{k+1} - \gamma_i^k + \beta_4 - \eta^k$, the linear system can be written as

$$\begin{bmatrix} A_1 + \beta_4 I & \beta_4 I & \beta_4 I & \cdots & \beta_4 I \\ \beta_4 I & A_2 + \beta_4 I & \beta_4 I & \cdots & \beta_4 I \\ \beta_4 I & \beta_4 I & A_3 + \beta_4 I & \cdots & \beta_4 I \\ \vdots & \vdots & \vdots & \ddots & \vdots \\ \beta_4 I & \beta_4 I & \beta_4 I & \cdots & A_N + \beta_4 I \end{bmatrix} \begin{bmatrix} z_1 \\ z_2 \\ z_3 \\ \vdots \\ z_N \end{bmatrix} = \begin{bmatrix} B_1 \\ B_2 \\ B_3 \\ \vdots \\ B_N \end{bmatrix}.$$

Let M be the coefficient matrix. For convenience, we will omit I in the following discussion. Let $\mathbf{1}$ denote the $N \times 1$ vector whose components are all 1, and let $J = \mathbf{1}\mathbf{1}^\top$. If we define the diagonal matrix

$$\tilde{D} = \operatorname{diag}(A_1, A_2, \ldots, A_N),$$

M can be written as

$$M = \tilde{D} + \beta_4 J.$$

Noting that $\tilde{D}$ is a diagonal matrix, we have

$$\tilde{D}^{-1} = \operatorname{diag}\left(\frac{1}{A_1}, \frac{1}{A_2}, \ldots, \frac{1}{A_N} \right).$$

Let

$$\mathbf{u} = \tilde{D}^{-1}\mathbf{1} = \left(\frac{1}{A_1}, \frac{1}{A_2}, \ldots, \frac{1}{A_N} \right)^\top,$$

$$S = \mathbf{1}^\top \tilde{D}^{-1}\mathbf{1} = \sum_{i=1}^{N} \frac{1}{A_i}.$$

Then we have

$$M^{-1} = \tilde{D}^{-1} - \frac{\beta_4}{1+\beta_4 S}\mathbf{u}\mathbf{u}^\top$$

by using the Sherman-Morrison formula. Specifically, for $i, j = 1, \ldots, N$,

$$(M^{-1})_{ij} = \begin{cases} \dfrac{1}{A_i} - \dfrac{\beta_4}{(1+\beta_4\sum_{i=1}^N 1/A_i)(A_i)^2}, & i = j, \\ -\dfrac{\beta_4}{(1+\beta_4\sum_{i=1}^N 1/A_i)A_iA_j}, & i \neq j. \end{cases}$$

Therefore, the solution of z_i is given as

$$\mathbf{z}^{k+1} = M^{-1}\begin{bmatrix} B_1 \\ B_2 \\ B_3 \\ \vdots \\ B_N \end{bmatrix}.$$

4.4.4. Updating v and w

The solution of v sub-problem (4.12) is given as

$$v^{k+1} = \mathcal{P}_{[0,1]}\left(\alpha_i^{k+1} - \frac{\eta_i^k}{\beta_3}\right),$$

where $\mathcal{P}_{[0,1]}(\cdot)$ is a projection on $[0,1]$. We then let

$$\begin{aligned} J_1 = \frac{1}{3}\sum_{i=1}^N \Big(&2U_1c_{i1}^{k+1} + 2U_2c_{i2}^{k+1} + 2U_3c_{i3}^{k+1} - U_1c_{i2}^{k+1} - U_1c_{i3}^{k+1} \\ &-U_2c_{i1}^{k+1} - U_2c_{i3}^{k+1} - U_3c_{i1}^{k+1} - U_3c_{i2}^{k+1}\Big)(z_i^{k+1})^p, \end{aligned}$$

$$J_2 = \frac{2}{3}\sum_{i=1}^N \left((c_{i1}^{k+1})^2 + (c_{i2}^{k+1})^2 + (c_{i3}^{k+1})^2 - c_{i1}^{k+1}c_{i2}^{k+1} - c_{i1}^{k+1}c_{i3}^{k+1} - c_{i2}^{k+1}c_{i3}^{k+1}\right)(z_i^{k+1})^p,$$

w sub-problem (4.13) can be rewritten as

$$w^{k+1} = \arg\min_w \frac{\lambda}{2}\int_\Omega \big(J_2w^2 - 2J_1w\big)dx + \frac{\beta_2}{2}\int_\Omega \left|w - g^{k+1} + \frac{\gamma^k}{\beta_2}\right|^2 dx.$$

The first order optimal condition is given as

$$\lambda(J_2w - J_1) + \beta_2\left(w - g^{k+1} + \frac{\gamma^k}{\beta_2}\right) = 0,$$

then

$$w^{k+1} = \frac{\lambda J_1 + \beta_2 g^{k+1} - \gamma^k}{\lambda J_2 + \beta_2}.$$

5. Experimental results

In this section, we evaluate the proposed model on both natural and artificial images. We compare it with several state-of-the-art segmentation methods, including: the SLaT model [2], the adaptive total variation (ATV) model [36], the soft segmentation model [18], the fuzzy Mumford-Shah model [16], and the saturation-component based fuzzy Mumford-Shah model [33].

In our proposed coordinate descent based algorithm, five parameters need to be specified: τ, θ are involved in α updating procedure. For all experiments, we set $\tau = 1$, $\theta = 0.1$. $\lambda, \rho_1, \rho_2, \mu$ are tuned individually for each experiment. For noisy images, we reduce λ because α requires stronger regularization. Since ρ_1 and μ influence the bias field, we decrease ρ_1 and increase μ for images with severe intensity inhomogeneity to enhance the effect of g. Finally, ρ_2 is adjusted to balance the contributions of hue and saturation similarity. The same parameter-tuning strategy is applied to the FMS and SFMS models. In our proposed ADMM based algorithm, the model related parameters $\lambda, \rho_1, \rho_2, \mu$ are set in the same way, the penalty parameters $\beta_1, \beta_2, \beta_3, \theta$ are all set to be 1, β_4 is set to be 1×10^{-5}, while increasing by 1.1 pre iteration for convergence. For the SLaT and ATV models, we use the default parameter settings provided in their respective papers. The convergence threshold ϵ in Algorithms 4.1 and 4.2 is set to 1×10^{-3}. The initialization $\mathbf{c}_i$ are randomly initialized. The maximum number of iterations is set to 500. The proposed algorithm is implemented in MATLAB, and all experiments are conducted on a PC equipped with a 13th Gen Intel(R) Core(TM) i5-13600KF 3.50 GHz CPU.

5.1. Comparison of the proposed algorithms

In this subsection, we discuss the efficiency of two proposed algorithms (coordinate descent based algorithm and ADMM based algorithm). We take the first image in Fig. 6 for example, which is a color image segmentation task with 5-phase. The related parameters are set to be the same, which is given in the caption of Fig. 6. We show the energy curves with respect to iterations in Fig. 2. It is clear that both algorithms are very efficient on solving the minimization problem. The corresponding energy of the two algorithms finally tends to be the same, which shows that the final results of the two algorithms are the same. Meanwhile, we see from the figure that ADMM based algorithm converges slightly faster then coordinate descent based algorithm.

Noting that ADMM usually converges faster when dealing with large-scale problems, we further resize the test image from 256×256 to 1024×1024, and display the energy curves with respect to iterations in Fig. 3. Again we see that ADMM based algorithm converges slightly faster then coordinate descent based algorithm, and the difference caused by image size is negligible.

We finally present the time consumption of different algorithms in Table 1. In summary, ADMM based algorithm and coordinate descent based algorithm have similar convergence speed and similar energy results, while ADMM based algorithm is more

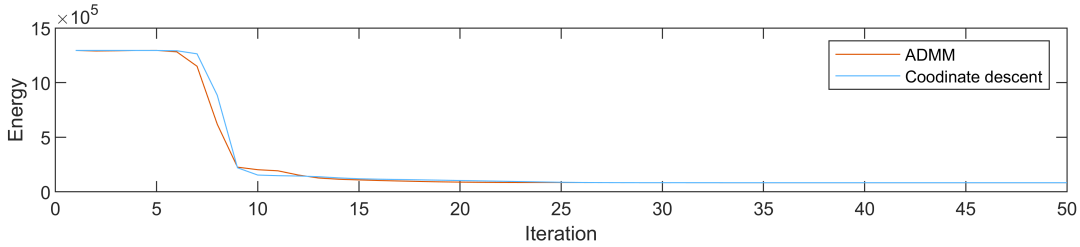

Figure 2: The energy curves with respect to iterations, image size is 256×256.

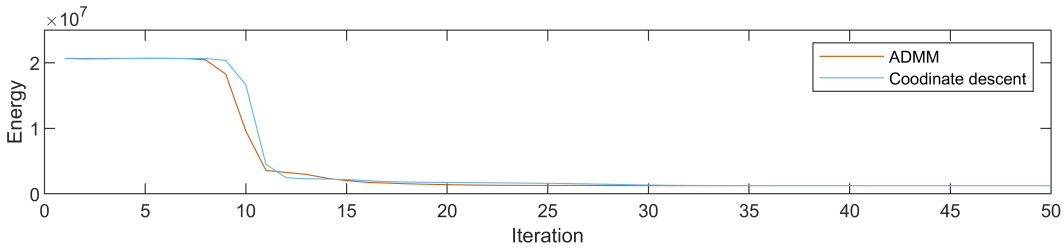

Figure 3: The energy curves with respect to iterations, image size is 1024×1024.

Table 1: Time consumption of different algorithms.

Method	Image size	Time (500 iterations)
ADMM	256×256	16.7400 s
Coordinate descent	256×256	6.4281 s
ADMM	1024×1024	265.8029 s
Coordinate descent	1024×1024	100.2480 s

time-consuming. Therefore, we use the proposed coordinate descent based algorithm to solve the proposed minimization problem in the following experiments.

5.2. Comparison of color image segmentation

In this experiment, we evaluate the proposed model for multi-phase color image segmentation on several test images. The input images and segmentation results are displayed in Figs. 4-6.

In Fig. 4, we show three examples of color image segmentation with 2-phase and 3-phase respectively. In the first row of Fig. 4, we test the performance of all methods under varying lighting conditions and provide 2-phase segmentation results for comparison. The competing methods (ATV, SCV, SLaT, FMS, SFMS) fail to separate the foreground (green region) from the background due to lighting variations. In contrast, the proposed HSF model achieves the expected segmentation. In the second row and third row of Fig. 4, we evaluate segmentation on images with gradual saturation changes. The other methods struggle to correctly segment all colors, but the HSF model succeeds by effectively balancing hue and saturation similarity.

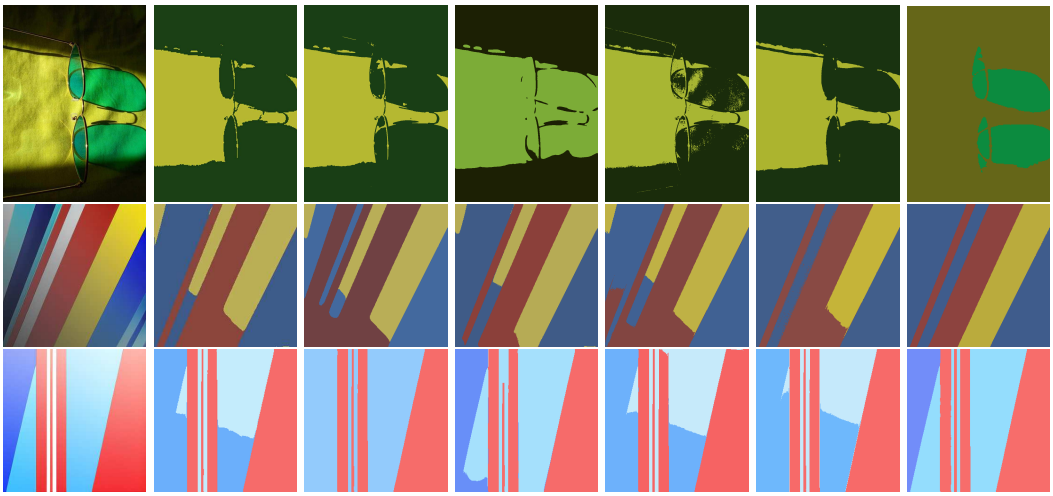

Figure 4: Left to right: the input image, the segmentation results by using ATV, SCV, SLaT, FMS, SFMS, and HSF of 2-phase (first row) and 3-phase (second and third rows) respectively. The parameters of HSF: $(\lambda, \rho_1, \rho_2, \mu) = (1\mathrm{e}-2, 1\mathrm{e}-3, 1\mathrm{e}2, 2\mathrm{e}5)$.

In Figs. 5 and 6, we show some examples of color image segmentation with 4-phase and 5-phase respectively. Both the SFMS and HSF models follow the color priority principle, which is advantageous for color segmentation. For example, in the first row of Fig. 5, the input color image mainly contains green, blue, and orange regions, dark boundaries, and the white background. The SFMS model and the proposed HSF model prioritize green and orange regions, while other methods incorrectly prioritize dark boundaries. We can also observe the color priority effect in the segmentation results of the second row in Fig. 5. But this time, the SFMS model fails to distinguish red from orange. The proposed HSF model correctly segments the red regions, demonstrating stronger hue sensitivity and robustness. Additional results in Figs. 5 and 6 further confirm the superiority of the HSF model over competing methods.

5.3. Synthetic color image segmentation

This experiment evaluates the proposed model's performance on synthetic color image segmentation. The input images and comparative segmentation results are presented in Figs. 7-21.

In Figs. 7, 12, and 17, we examine segmentation performance under gradual saturation changes along vertical and diagonal directions, where saturation is degraded by multiplying itself with linear weights in $[0.3, 0.9]$. Comparative results from ATV, SCV, SLaT, FMS, SFMS, and HSF methods demonstrate that only the proposed HSF model maintains accurate color segmentation across all phase scenarios. As shown in Fig. 17, conventional methods fail to properly segment yellow, light orange, and orange regions, while HSF produces correct segmentation boundaries.

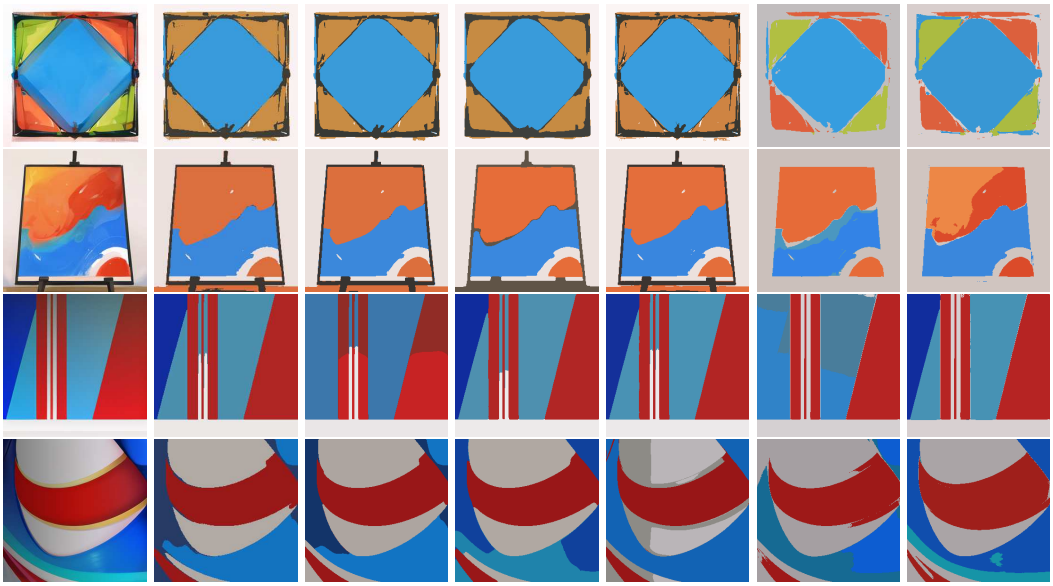

Figure 5: Left to right: the input image, the segmentation results by using ATV, SCV, SLaT, FMS, SFMS, and HSF of 4-phase respectively. The parameters of HSF: $(\lambda, \rho_1, \rho_2, \mu) = (1\mathrm{e}-2, 1\mathrm{e}-3, 1\mathrm{e}2, 2\mathrm{e}5)$.

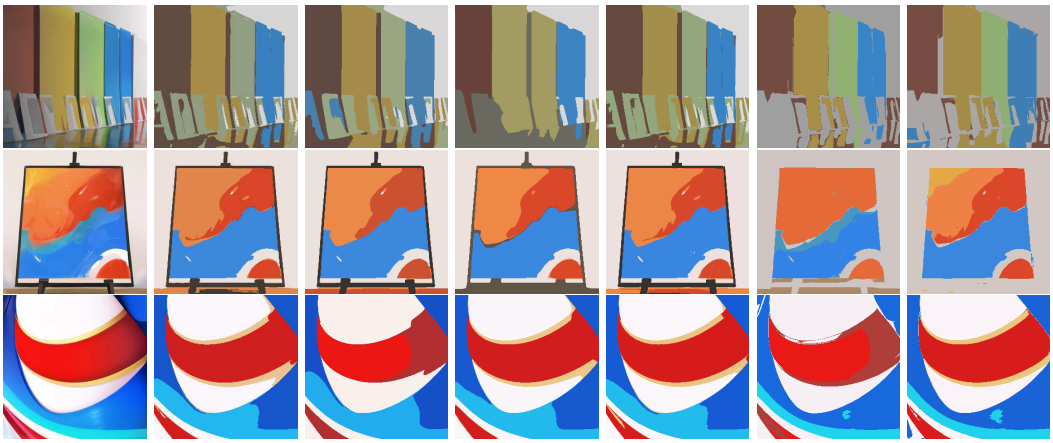

Figure 6: Left to right: the input image, the segmentation results by using ATV, SCV, SLaT, FMS, SFMS, and HSF of 5-phase respectively. The parameters of HSF: $(\lambda, \rho_1, \rho_2, \mu) = (1\mathrm{e}-2, 1\mathrm{e}-3, 1\mathrm{e}2, 2\mathrm{e}5)$.

Similar tests are conducted for gradual value changes (Figs. 8, 13, 18) and combined saturation-value variations (Figs. 9, 14, 19). Using the same degradation methodology, HSF consistently outperformed other methods. Notably in Figs. 18-19, while conventional methods produce incorrect segmentation of warm-color regions (yellow/orange), HSF maintained accurate results regardless of value or combined variations.

We further test the impulse noisy conditions where saturation is corrupted by random multipliers in $[0.3, 1.2]$ (Figs. 10, 15, 20), and value components are similarly de-

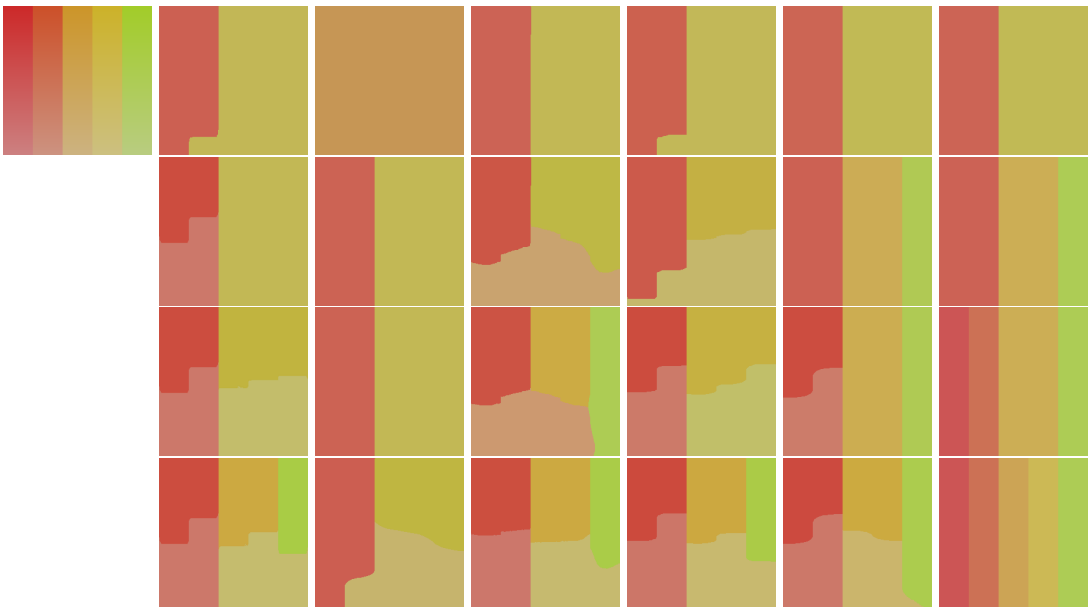

Figure 7: Left to right: the input image, the segmentation results by using ATV, SCV, SLaT, FMS, SFMS, and HSF respectively; Top to bottom: the segmentation results of 2, 3, 4, 5-phase respectively. The parameters of HSF: $(\lambda, \rho_1, \rho_2, \mu) = (2\mathrm{e}-4, 1\mathrm{e}-3, 5\mathrm{e}3, 2\mathrm{e}5)$.

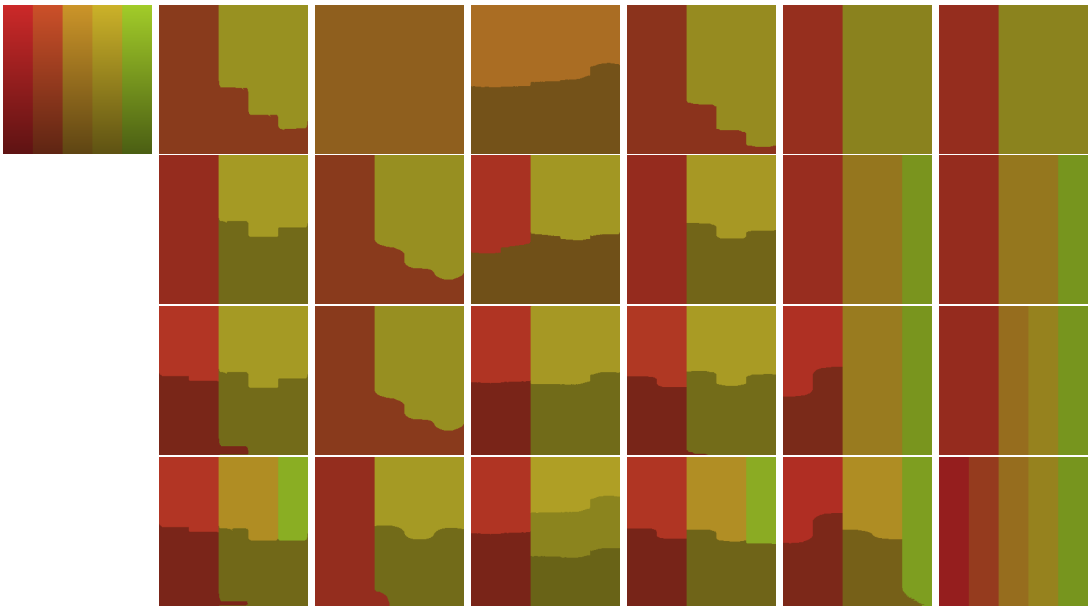

Figure 8: Left to right: the input image, the segmentation results by using ATV, SCV, SLaT, FMS, SFMS, and HSF respectively. Top to bottom: the segmentation results of 2, 3, 4, 5-phase respectively. The parameters of HSF: $(\lambda, \rho_1, \rho_2, \mu) = (2\mathrm{e}-4, 1\mathrm{e}-3, 5\mathrm{e}3, 2\mathrm{e}5)$.

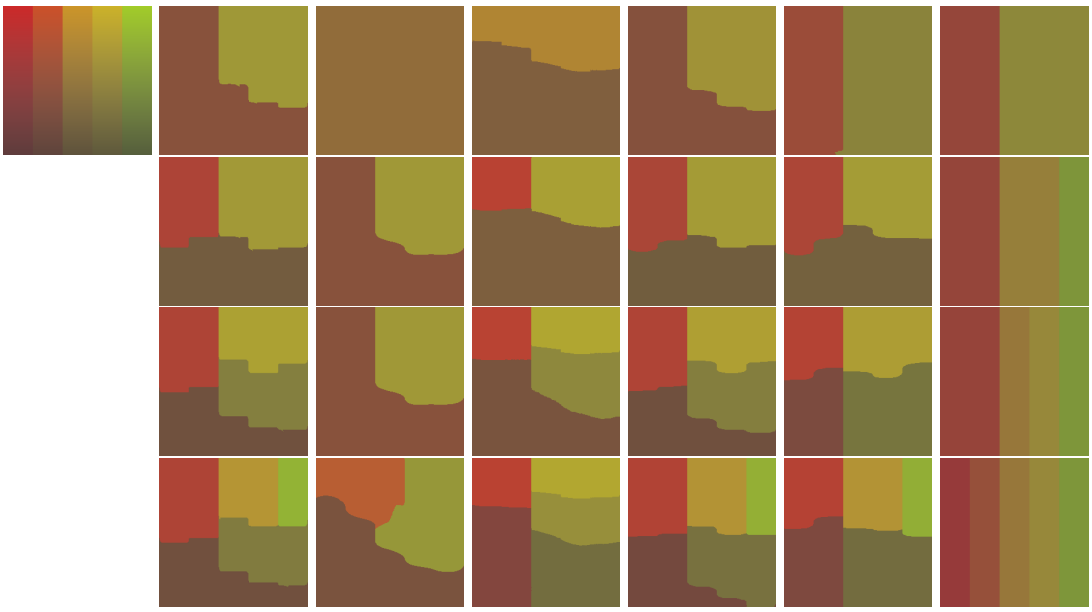

Figure 9: Left to right: the input image, the segmentation results by using ATV, SCV, SLaT, FMS, SFMS, and HSF respectively. Top to bottom: the segmentation results of 2, 3, 4, 5-phase respectively. The parameters of HSF: $(\lambda, \rho_1, \rho_2, \mu) = (2\mathrm{e}-4, 1\mathrm{e}-3, 5\mathrm{e}3, 2\mathrm{e}5)$.

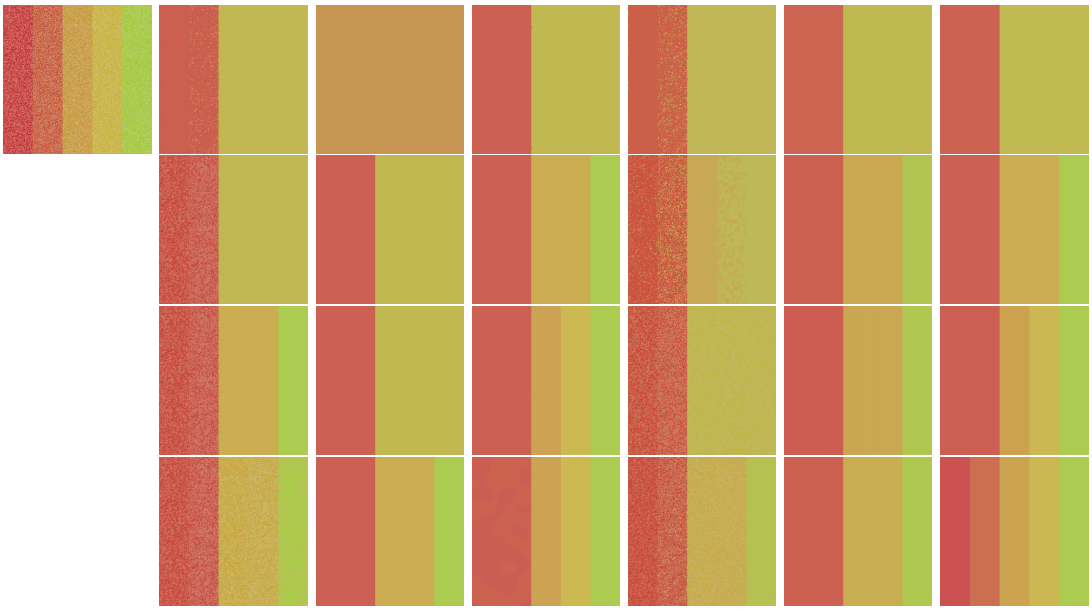

Figure 10: Left to right: the input image, the segmentation results by using ATV, SCV, SLaT, FMS, SFMS, and HSF respectively. Top to bottom: the segmentation results of 2, 3, 4, 5-phase respectively. The parameters of HSF: $(\lambda, \rho_1, \rho_2, \mu) = (2\mathrm{e}-4, 1\mathrm{e}-3, 5\mathrm{e}3, 2\mathrm{e}5)$.

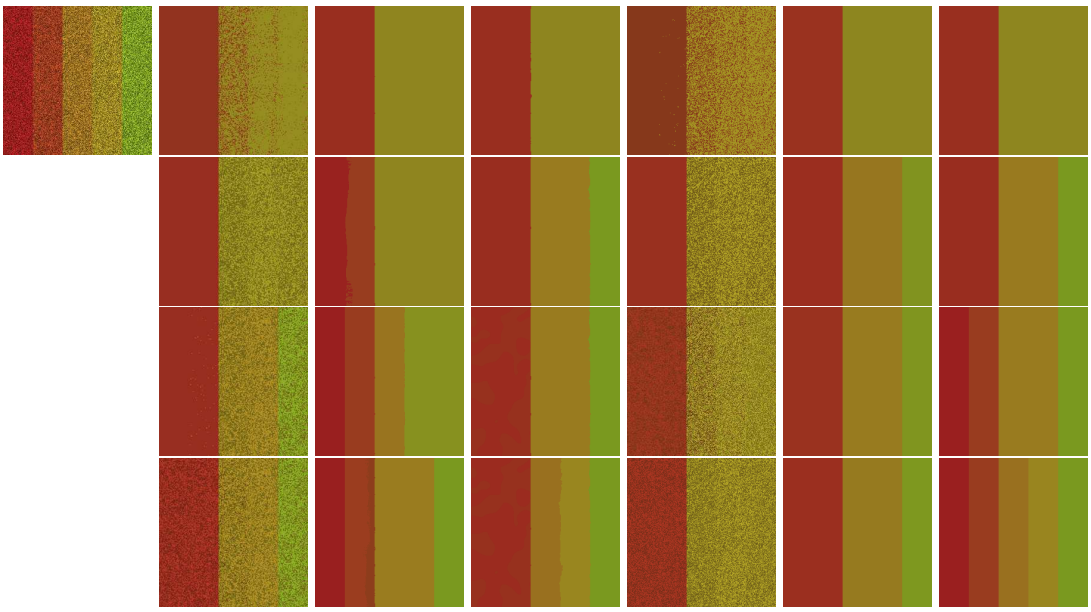

Figure 11: Left to right: the input image, the segmentation results by using ATV, SCV, SLaT, FMS, SFMS, and HSF respectively. Top to bottom: the segmentation results of 2, 3, 4, 5-phase respectively. The parameters of HSF: $(\lambda, \rho_1, \rho_2, \mu) = (2\mathrm{e}-4, 1\mathrm{e}-3, 5\mathrm{e}3, 2\mathrm{e}5)$.

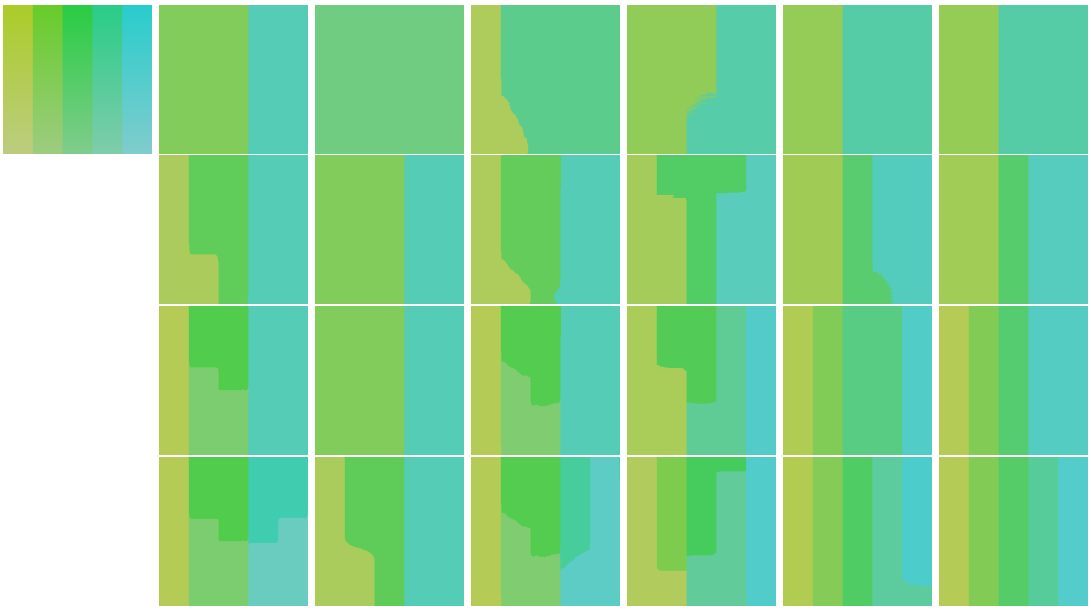

Figure 12: Left to right: the input image, the segmentation results by using ATV, SCV, SLaT, FMS, SFMS, and HSF respectively. Top to bottom: the segmentation results of 2, 3, 4, 5-phase respectively. The parameters of HSF: $(\lambda, \rho_1, \rho_2, \mu) = (2\mathrm{e}-4, 1\mathrm{e}-3, 5\mathrm{e}3, 2\mathrm{e}5)$.

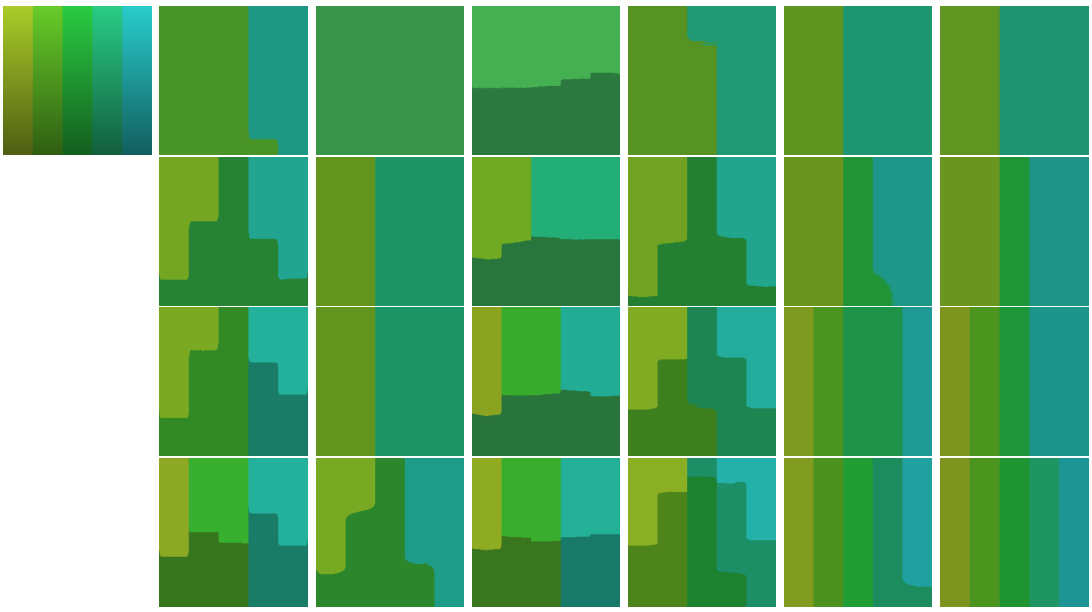

Figure 13: Left to right: the input image, the segmentation results by using ATV, SCV, SLaT, FMS, SFMS, and HSF respectively. Top to bottom: the segmentation results of 2, 3, 4, 5-phase respectively. The parameters of HSF: $(\lambda, \rho_1, \rho_2, \mu) = (2\mathrm{e}-4, 1\mathrm{e}-3, 5\mathrm{e}3, 2\mathrm{e}5)$.

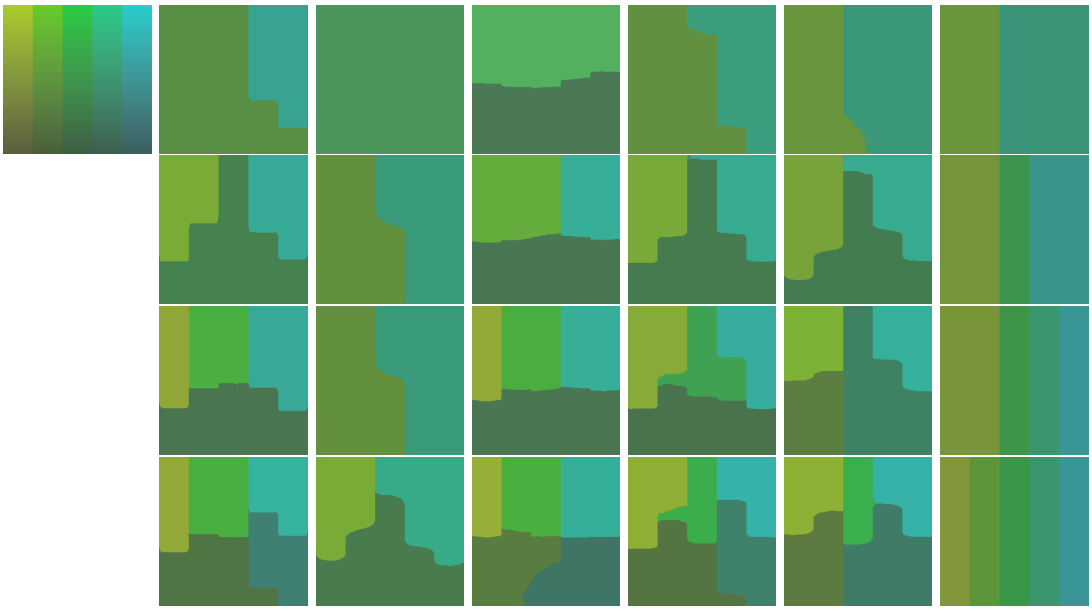

Figure 14: Left to right: the input image, the segmentation results by using ATV, SCV, SLaT, FMS, SFMS, and HSF respectively. Top to bottom: the segmentation results of 2, 3, 4, 5-phase respectively. The parameters of HSF: $(\lambda, \rho_1, \rho_2, \mu) = (2\mathrm{e}-4, 1\mathrm{e}-3, 5\mathrm{e}3, 2\mathrm{e}5)$.

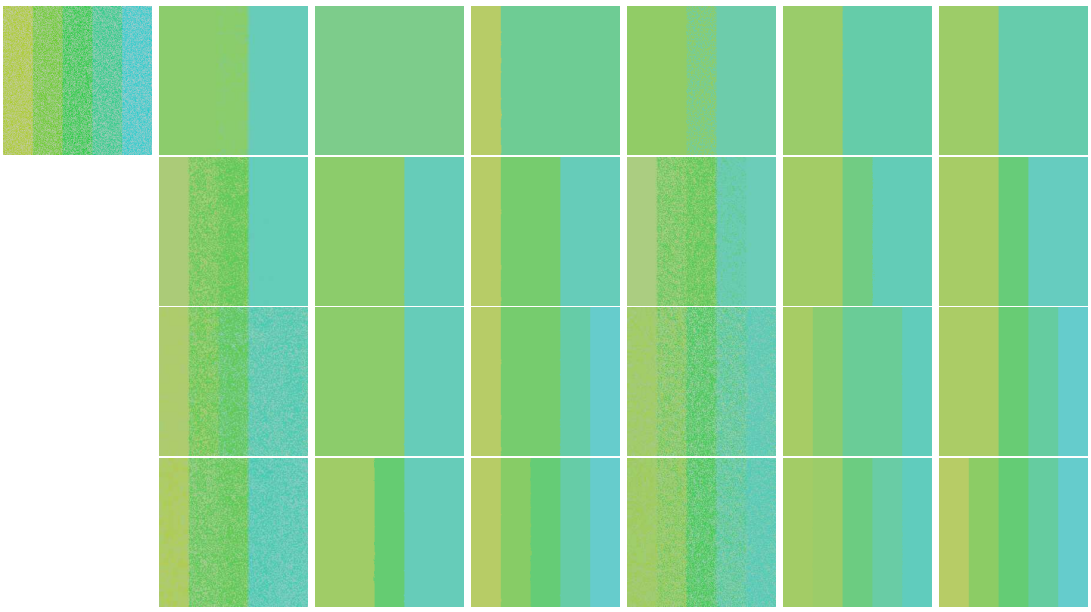

Figure 15: Left to right: the input image, the segmentation results by using ATV, SCV, SLaT, FMS, SFMS, and HSF respectively. Top to bottom: the segmentation results of 2, 3, 4, 5-phase respectively. The parameters of HSF: $(\lambda, \rho_1, \rho_2, \mu) = (2\mathrm{e}-4, 1\mathrm{e}-3, 5\mathrm{e}3, 2\mathrm{e}5)$.

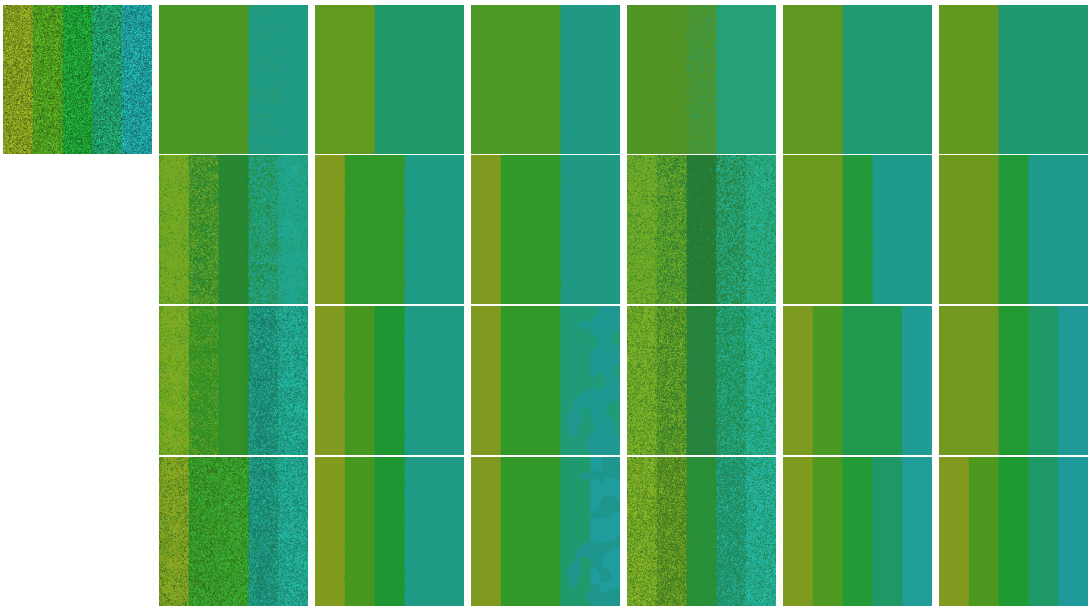

Figure 16: Left to right: the input image, the segmentation results by using ATV, SCV, SLaT, FMS, SFMS, and HSF respectively. Top to bottom: the segmentation results of 2, 3, 4, 5-phase respectively. The parameters of HSF: $(\lambda, \rho_1, \rho_2, \mu) = (2\mathrm{e}-4, 1\mathrm{e}-3, 5\mathrm{e}3, 2\mathrm{e}5)$.

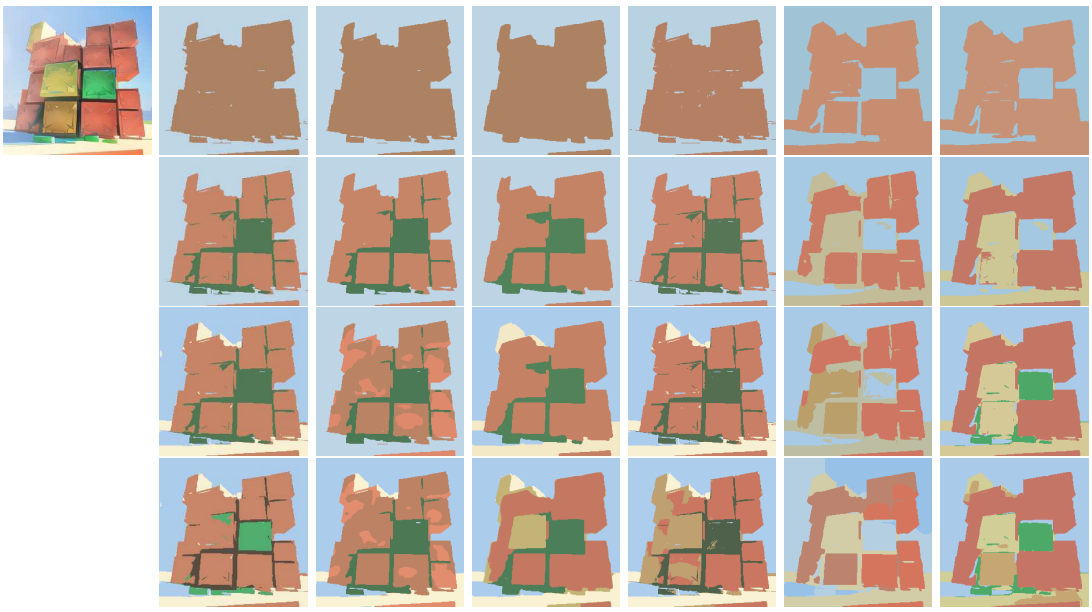

Figure 17: Left to right: the input image, the segmentation results by using ATV, SCV, SLaT, FMS, SFMS, and HSF respectively. Top to bottom: the segmentation results of 2, 3, 4, 5-phase respectively. The parameters of HSF: $(\lambda, \rho_1, \rho_2, \mu) = (2\mathrm{e}-4, 1\mathrm{e}-3, 5\mathrm{e}3, 2\mathrm{e}5)$.

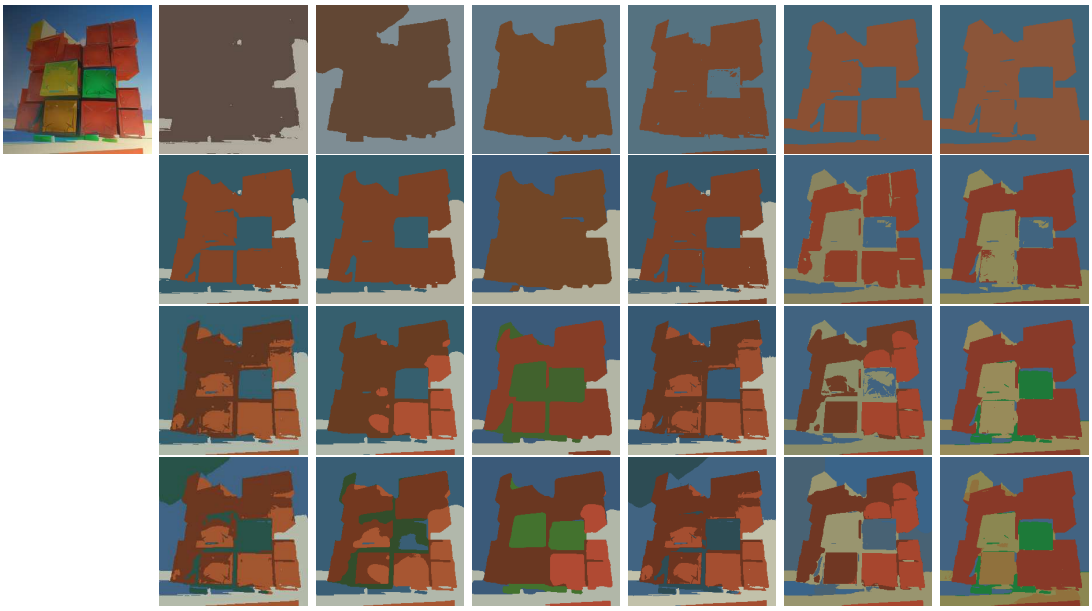

Figure 18: Left to right: the input image, the segmentation results by using ATV, SCV, SLaT, FMS, SFMS, and HSF respectively. Top to bottom: the segmentation results of 2, 3, 4, 5-phase respectively. The parameters of HSF: $(\lambda, \rho_1, \rho_2, \mu) = (2\mathrm{e}-4, 1\mathrm{e}-3, 5\mathrm{e}3, 2\mathrm{e}5)$.

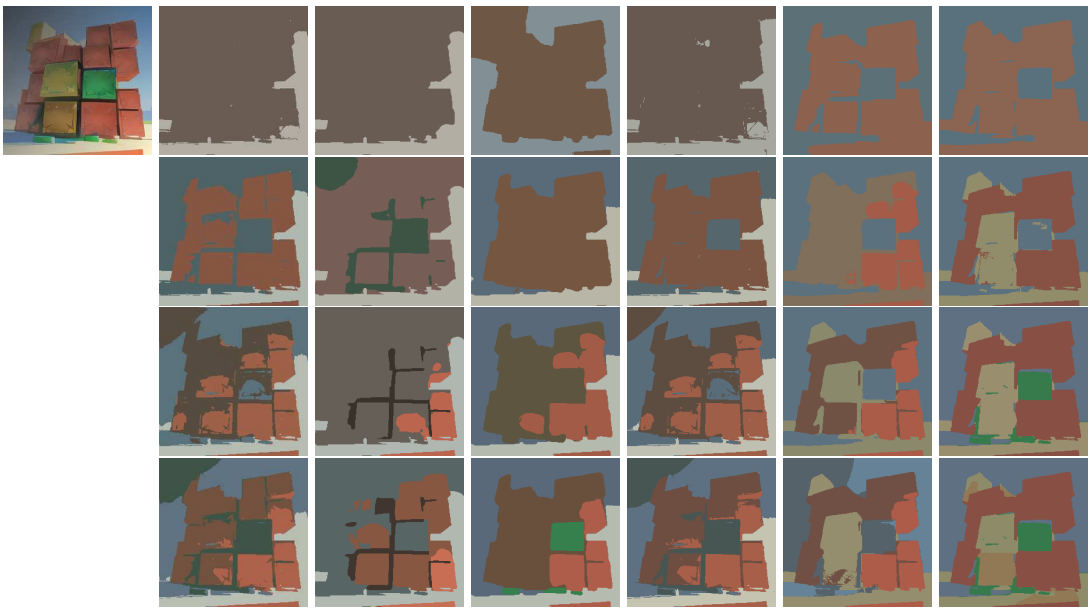

Figure 19: Left to right: the input image, the segmentation results by using ATV, SCV, SLaT, FMS, SFMS, and HSF respectively. Top to bottom: the segmentation results of 2, 3, 4, 5-phase respectively. The parameters of HSF: $(\lambda, \rho_1, \rho_2, \mu) = (2\mathrm{e}-4, 1\mathrm{e}-3, 5\mathrm{e}3, 2\mathrm{e}5)$.

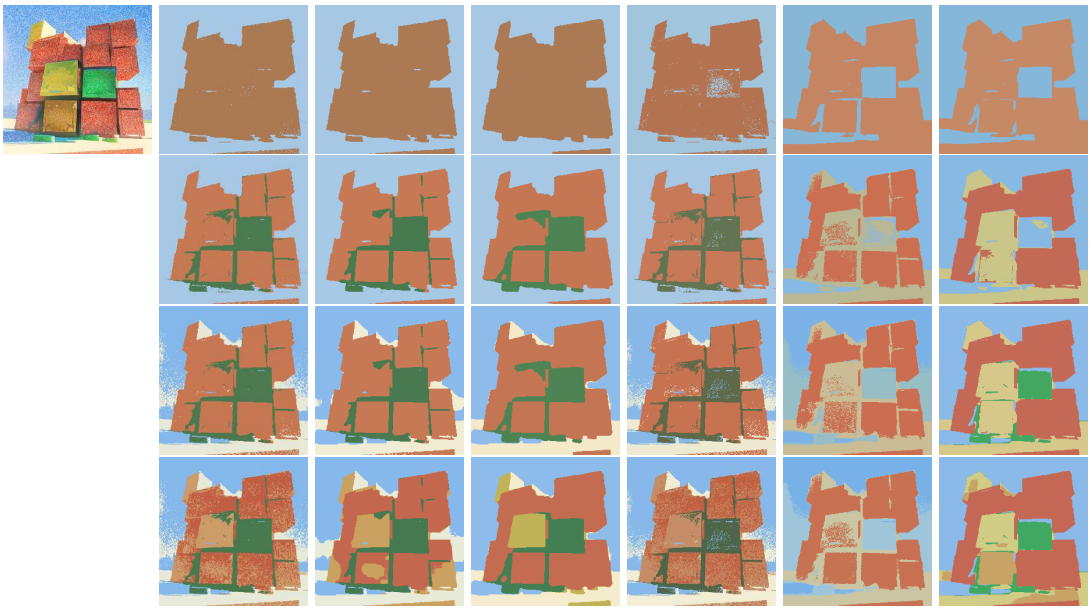

Figure 20: Left to right: the input image, the segmentation results by using ATV, SCV, SLaT, FMS, SFMS, and HSF respectively. Top to bottom: the segmentation results of 2, 3, 4, 5-phase respectively. The parameters of HSF: $(\lambda, \rho_1, \rho_2, \mu) = (2\mathrm{e}-4, 1\mathrm{e}-3, 5\mathrm{e}3, 2\mathrm{e}5)$.

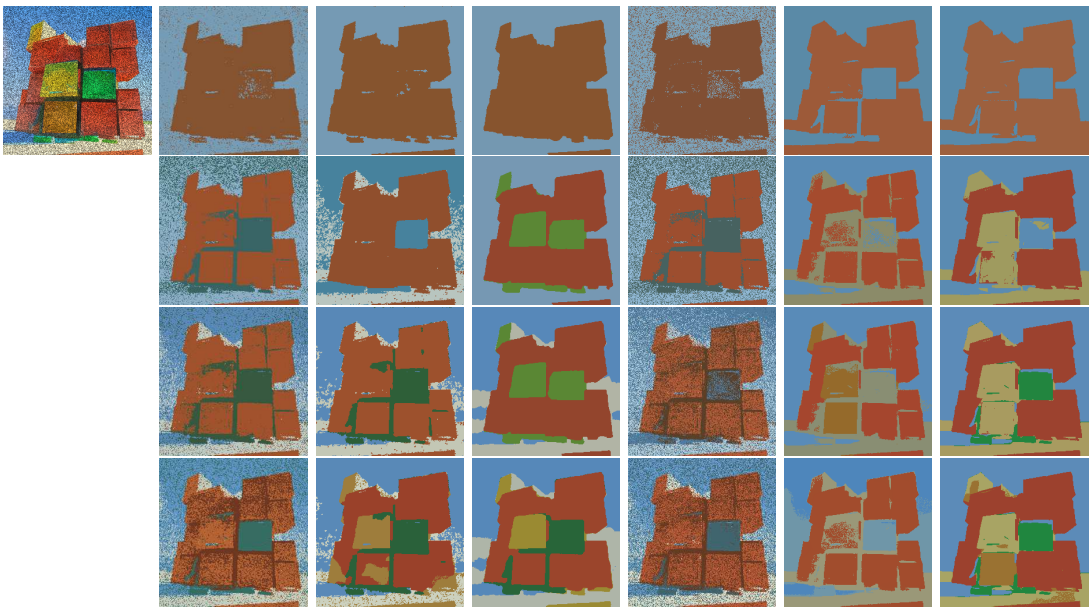

Figure 21: Left to right: the input image, the segmentation results by using ATV, SCV, SLaT, FMS, SFMS, and HSF respectively. Top to bottom: the segmentation results of 2, 3, 4, 5-phase respectively. The parameters of HSF: $(\lambda, \rho_1, \rho_2, \mu) = (2\mathrm{e}-4, 1\mathrm{e}-3, 5\mathrm{e}3, 2\mathrm{e}5)$.

graded (Figs. 11, 16, 21). Comparative results reveal that conventional methods exhibit two key limitations: color misclassification (e.g., yellow/orange regions in Figs. 20-21) and noise-sensitive artifacts (particularly in ATV, SCV, FMS, SFMS outputs). In contrast, HSF demonstrates superior noise robustness, maintaining both accurate color segmentation and clean boundary delineation across all test cases.

5.4. Natural color image segmentation

This experiment evaluates the proposed model's performance for color image segmentation on natural images. The input images and comparative segmentation results with varying phase numbers are presented in Figs. 22-25. The results demonstrate that the proposed HSF model exhibits superior color sensitivity due to its effective hue similarity formulation. As shown in Fig. 22, the model correctly separates the foreground flower region from the background, achieving the desired segmentation. In contrast, ATV, SCV, FMS, and SFMS models fail to properly segment the red, yellow, and background regions in 3-phase segmentation, the SLaT model incorrectly segments the background region in 5-phase segmentation. Similar advantages are observed in other test cases: red flower segmentation (Fig. 23), tiger and red region separation (Fig. 24), lotus and stamen (Fig. 25). While all comparative methods (ATV, SCV, SLaT, FMS, SFMS) produce unsatisfactory results across different phase settings, the HSF model consistently achieves segmentation that aligns perfectly with our color-based segmentation objectives.

Figure 22: Left to right: the input image, the segmentation results by using ATV, SCV, SLaT, FMS, SFMS, and HSF respectively; Top to bottom: the segmentation results of 2, 3, 4, 5-phase respectively. The parameters of HSF: $(\lambda, \rho_1, \rho_2, \mu) = (1\mathrm{e}-2, 1\mathrm{e}-3, 1\mathrm{e}2, 2\mathrm{e}5)$.

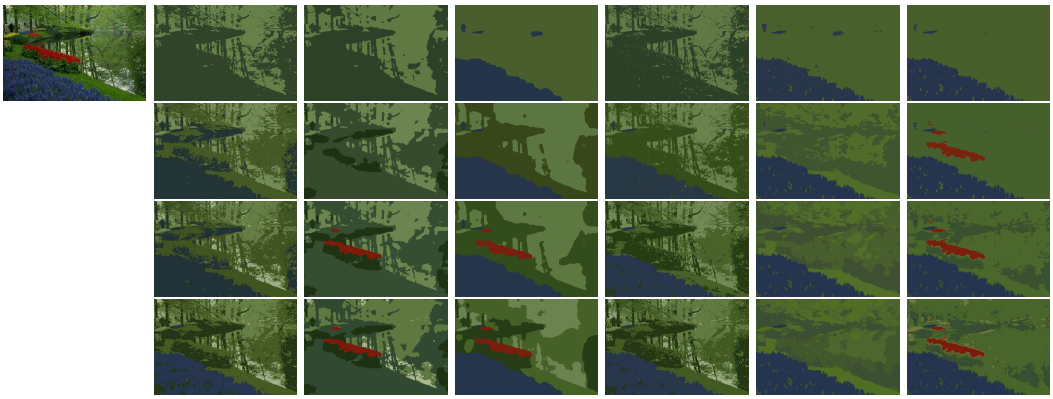

Figure 23: Left to right: the input image, the segmentation results by using ATV, SCV, SLaT, FMS, SFMS, and HSF respectively; Top to bottom: the segmentation results of 2, 3, 4, 5-phase respectively. The parameters of HSF: $(\lambda, \rho_1, \rho_2, \mu) = (5\mathrm{e}-3, 1\mathrm{e}-3, 5\mathrm{e}2, 2\mathrm{e}5)$.

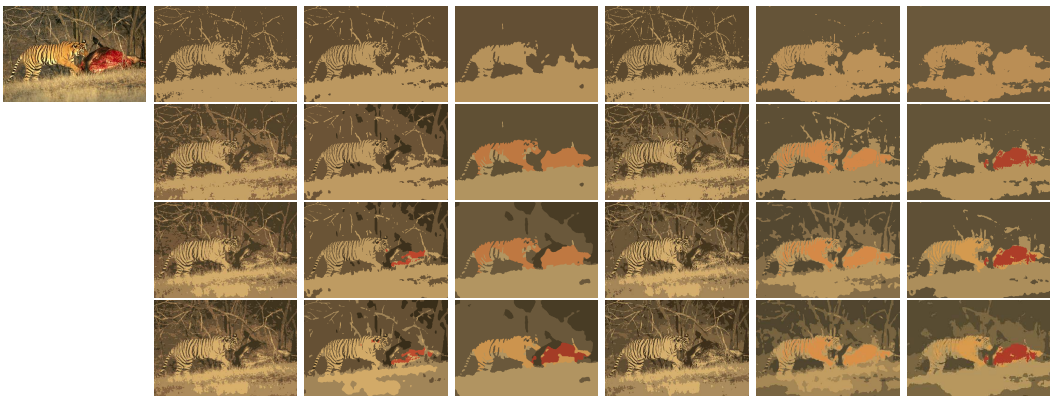

Figure 24: Left to right: the input image, the segmentation results by using ATV, SCV, SLaT, FMS, SFMS, and HSF respectively; Top to bottom: the segmentation results of 2, 3, 4, 5-phase respectively. The parameters of HSF: $(\lambda, \rho_1, \rho_2, \mu) = (1\mathrm{e}-2, 1\mathrm{e}-3, 1\mathrm{e}2, 2\mathrm{e}5)$.

Figure 25: Left to right: the input image, the segmentation results by using ATV, SCV, SLaT, FMS, SFMS, and HSF respectively; Top to bottom: the segmentation results of 2, 3, 4, 5-phase respectively. The parameters of HSF: $(\lambda, \rho_1, \rho_2, \mu) = (1\mathrm{e}-2, 1\mathrm{e}-3, 1\mathrm{e}2, 2\mathrm{e}5)$.

6. Concluding remarks

In this paper, we develop a novel variational model for color image segmentation based on hue-saturation similarity. Color image segmentation is highly related to hue and saturation channels of HSV color space which contains more intuitive color information than RGB color space. Therefore, we make use of hue-saturation similarity and the idea of fuzzy membership function to formulate a variational model for color image segmentation. Specifically, we first propose the definitions of the hue distance and saturation distance to describe hue-saturation similarity. We then formulate a novel data fitting method with an adaptive weight coefficient by using hue-saturation similarity in the proposed energy functional. We also consider the influence of bias field in the saturation component. Efficient iterative algorithms including coordinate descent and ADMM have been proposed for solving the proposed optimization problem.

The existence of the solution of the proposed model and the convergence of the proposed coordinate descent algorithm has been studied at the same time. We have conducted extensive numerical experiments on several synthetic images and natural images with different kinds of degradation to test the robustness of proposed model. The displayed examples effectively demonstrate the advantage of the proposed model for color segmentation compared with other testing color image segmentation methods. The proposed model demonstrates the superiority of hue-saturation similarity in color image segmentation, and provides a novel extension to the idea of fuzzy membership

function. We consider the following future research topics:

1 In this paper, we focus on color image segmentation problem. It would be very interesting to further study hue-saturation distance/similarity/regularization for different image processing problems, such as color image restoration, color image inpainting, etc.

2 Noting that the proposed hue distance is nonlinear, which poses a challenge to the design of the numerical algorithms. In the future, we will consider appropriate linearization methods to handle the hue channel and to improve the computational efficiency.

3 It would be very interesting to consider specific targets tracking in videos based on hue-saturation similarity.

Acknowledgements

The research of W. Wang is supported by the Natural Science Foundation of Shanghai (Grant No. 22ZR1465300).

References

[1] X. BRESSON, S. ESEDOḠLU, P. VANDERGHEYNST, J.-P. THIRAN, AND S. OSHER, *Fast global minimization of the active contour/snake model*, J. Math. Imaging Vis. 28 (2007), 151–167.

[2] X. CAI, R. CHAN, M. NIKOLOVA, AND T. ZENG, *A three-stage approach for segmenting degraded color images: Smoothing, lifting and thresholding (slat)*, J. Sci. Comput. 72 (2017), 1313–1332.

[3] X. CAI, R. CHAN, C.-B. SCHONLIEB, G. STEIDL, AND T. ZENG, *Linkage between piecewise constant Mumford-Shah model and Rudin-Osher-Fatemi model and its virtue in image segmentation*, SIAM J. Sci. Comput. 41 (2019), B1310–B1340.

[4] X. CAI, R. CHAN, AND T. ZENG, *A two-stage image segmentation method using a convex variant of the Mumford-Shah model and thresholding*, SIAM J. Imaging Sci. 6 (2013), 368–390.

[5] V. CASELLES, R. KIMMEL, AND G. SAPIRO, *Geodesic active contours*, Int. J. Comput. Vis. 22 (1997), 61–79.

[6] A. CHAMBOLLE, D. CREMERS, AND T. POCK, *A convex approach to minimal partitions*, SIAM J. Imaging Sci. 5 (2012), 1113–1158.

[7] R. CHAN, H. YANG, AND T. ZENG, *A two-stage image segmentation method for blurry images with poisson or multiplicative gamma noise*, SIAM J. Imaging Sci. 7 (2014), 98–127.

[8] T. F. CHAN, S. ESEDOGLU, AND M. NIKOLOVA, *Algorithms for finding global minimizers of image segmentation and denoising models*, SIAM J. Appl. Math. 66 (2006), 1632–1648.

[9] T. F. CHAN AND L. A. VESE, *Active contours without edges*, IEEE Trans. Image Process. 10 (2001), 266–277.

[10] D. CREMERS, M. ROUSSON, AND R. DERICHE, *A review of statistical approaches to level set segmentation: Integrating color, texture, motion and shape*, Int. J. Comput. Vis. 72 (2007), 195–215.
[11] E. ELHAMIFAR AND R. VIDAL, *Sparse subspace clustering: Algorithm, theory, and applications*, IEEE Trans. Pattern Anal. Mach. Intell. 35 (2013), 2765–2781.
[12] L. GRADY AND C. ALVINO, *Reformulating and optimizing the Mumford-Shah functional on a graph - A faster, lower energy solution*, in: Lecture Notes in Computer Science, Springer 5302 (2008), 248–261.
[13] N. HOUHOU, J.-P. THIRAN, AND X. BRESSON, *Fast texture segmentation model based on the shape operator and active contour*, in: Proceedings of the 2008 IEEE Conference on Computer Vision and Pattern Recognition, (2008), 1–8.
[14] Z. JIA, M. K. NG, AND W. WANG, *Color image restoration by saturation-value total variation*, SIAM J. Imaging Sci. 12 (2019), 972–1000.
[15] C. LI, R. HUANG, Z. DING, C. GATENBY, D. METAXAS, AND J. GORE, *A variational level set approach to segmentation and bias correction of images with intensity inhomogeneity*, in: Medical Image Computing and Computer-Assisted Intervention – MICCAI 2008. Lecture Notes in Computer Science, Springer 5242 (2008), 1083–1091.
[16] F. LI, M. K. NG, AND C. LI, *Variational fuzzy Mumford-Shah model for image segmentation*, SIAM J. Appl. Math. 70 (2010), 2750–2770.
[17] F. LI, M. K. NG, T. Y. ZENG, AND C. SHEN, *A multiphase image segmentation method based on fuzzy region competition*, SIAM J. Imaging Sci. 3 (2010), 277–299.
[18] F. LI, C. SHEN, AND C. LI, *Multiphase soft segmentation with total variation and h1 regularization*, J. Math. Imaging Vision 37 (2010), 98–111.
[19] X. LI, X. YANG, AND T. ZENG, *A three-stage variational image segmentation framework incorporating intensity inhomogeneity information*, SIAM J. Imaging Sci. 13 (2020), 1692–1715.
[20] R. LUKAC AND K. N. PLATANIOTIS, *Color Image Processing: Methods and Applications*, CRC Press, 2018.
[21] Q. MA AND D. KONG, *A new variational model for joint restoration and segmentation based on the Mumford-Shah model*, J. Vis. Commun. Image Represent 53 (2018), 224–234.
[22] B. MORY AND R. ARDON, *Fuzzy region competition: A convex two-phase segmentation framework*, in: Scale Space and Variational Methods in Computer Vision. Lecture Notes in Computer Science, Springer 4485 (2007), 214–226.
[23] D. MUMFORD AND J. SHAH, *Boundary detection by minimizing functionals*, in: Proceedings of the IEEE Conference on Computer Vision and Pattern Recognition, 17 (1985), 137–154.
[24] D. B. MUMFORD AND J. SHAH, *Optimal approximations by piecewise smooth functions and associated variational problems*, Comm. Pure Appl. Math. 42 (1989), 577—685.
[25] N. PARAGIOS AND R. DERICHE, *Geodesic active regions for supervised texture segmentation*, in: Proceedings of the Seventh IEEE International Conference on Computer Vision, 2 (1999), 926–932.
[26] D. L. PHAM AND J. L. PRINCE, *An adaptive fuzzy c-means algorithm for image segmentation in the presence of intensity inhomogeneities*, Pattern Recognit. Lett. 20 (1999), 57–68.
[27] A. PLAZA ET AL., *Recent advances in techniques for hyperspectral image processing*, Remote Sens. Environ. 113 (2009), S110–S122.
[28] J.-P. SONG AND S.-J. LI, *An improved Mumford-Shah model and its applications to image processing with the piecewise constant level set method*, Acta Autom. Sin. 33 (2007), 1259–1262.

[29] H. SUN, L. LIU, AND F. LI, *A Lie group semi-supervised fcm clustering method for image segmentation*, Pattern Recognit. 155 (2024), Paper No. 110681.
[30] D. TOWNSEND, *Multimodality imaging of structure and function*, Phys. Med. Biol. 53 (2008), R1–R39.
[31] A. VITTI, *The Mumford-Shah variational model for image segmentation: An overview of the theory, implementation and use*, ISPRS J. Photogramm. Remote Sens. 69 (2012), 50–64.
[32] H.-Y. WANG, F. CHEN, A. BRUM, AND C.-X. SHI, *Classification of small structures in piecewise-constant Mumford-Shah model*, Neurocomputing 269 (2017), 132–141.
[33] W. WANG, C. LI, AND M. K. NG, *A saturation-component based fuzzy Mumford-Shah model for color image segmentation*, CSIAM Trans. Appl. Math. 2 (2021), 724–747.
[34] W. WANG AND C. YANG, *Total variations for hue, saturation, and value of a color image*, CSIAM Trans. Appl. Math. 5 (2024), 551–589.
[35] C. WU AND J. ZHAO, *Joint learning framework of superpixel generation and fuzzy sparse subspace clustering for color image segmentation*, Signal Process. 222 (2024), Paper No. 109515.
[36] T. WU, X. GU, Y. WANG, AND T. ZENG, *Adaptive total variation based image segmentation with semi-proximal alternating minimization*, Signal Process. 183 (2021), Paper No. 108017.
[37] P. XUE AND S. NIU, *A novel active contour model based on features for image segmentation*, Pattern Recognit. 155 (2024), Paper No. 110673.
[38] Y. YANG, Q. ZHONG, Y. DUAN, AND T. ZENG, *A weighted bounded Hessian variational model for image labeling and segmentation*, Signal Process. 173 (2020), Paper No. 107564.
[39] S. C. ZHU AND A. YUILLE, *Region competition: Unifying snakes, region growing, and bayes/mdl for multiband image segmentation*, IEEE Trans. Pattern Anal. Mach. Intell. 18 (1996), 884–900.
[40] Y. ZHU, X. XIU, W. LIU, AND C. YIN, *Joint sparse subspace clustering via fast l2,0-norm constrained optimization*, Expert Syst. Appl. 265 (2025), Paper No. 125845.